Available online at www.sciencedirect.com
ScienceDirect
Comput. Methods Appl. Mech. Engrg. 365 (2020) 113033
Computer methods in applied mechanics and engineering
www.elsevier.com/locate/cma

Enriched Isogeometric Collocation for two-dimensional time-harmonic acoustics

Tomás Ayala[a], Javier Videla[b], Cosmin Anitescu[c], Elena Atroshchenko[b,*]

[a] Department of Mechanical Engineering, University of Chile, Santiago 8370448, Chile
[b] School of Civil and Environmental Engineering, University of New South Wales, Sydney, Australia
[c] Institute of Structural Mechanics, Bauhaus-Universität Weimar, Weimar, Germany

Received 15 November 2019; received in revised form 23 March 2020; accepted 23 March 2020
Available online 11 April 2020

Abstract

In this work, the isogeometric collocation (IGA-C) is paired with two types of enrichment: Plane Wave (PW-) and Generalized Harmonic Polynomial (GHP-) functions, to solve 2D-problems for the Helmholtz equation. A parametric study is conducted, and a detailed assessment of the performance of the method in a number of benchmark problems is provided. Three different collocation methods are tested for the non-enriched formulation, namely Greville abscissae (GA), Approximated Cauchy–Galerkin (ACG) and Superconvergent (SC) points, showing that the ACG scheme is the best choice in terms of overall error, convergence rate and ease of solving the linear system. Then, the influence of the number of shape functions in the original and enriched basis, location and number of collocation points and wave-number over both the convergence rate as well as the condition number of the stiffness matrix are studied. The numerical results show that: (1) there is an improvement over the non-enriched formulation, (2) the improvement depends on the choice of the number and type of enrichment, and (3) The pollution error is not completely alleviated with the enriched formulations.

Keywords: Isogeometric; Collocation method; Plane-wave enrichment; Generalized harmonic polynomial enrichment; Partition of unity

1. Introduction

Boundary value problems for the Helmholtz equation appear in a wide range of applications, concerned with analysis of wave propagation (e.g. time-harmonic acoustics identification of kidney stones by medical imaging [1], optimization of micro-acoustic devices ranging from hearing aids to meta-materials [2], or radar cross section reduction [3], etc.). The Helmholtz equation is given by:

$$\Delta u + k^2 u = 0, \tag{1}$$

Nowadays, various advanced numerical methods have been developed for the Helmholtz equation, aiming to minimize numerical error at optimal computational cost. The following three main sources of numerical error can be identified:

* Corresponding author.
E-mail address: e.atroshchenko@unsw.edu.au (E. Atroshchenko).

https://doi.org/10.1016/j.cma.2020.113033

- Discretization error, occurring when the solution (and the computational domain in finite elements methods) are approximated with shape functions
- The pollution or numerical dispersion error [4–6], associated with high wave numbers
- Boundary truncation error for problems in unbounded domains

The first two aspects will be discussed in detail in the following sections. The boundary truncation error appears in finite element and other domain-type methods in unbounded domains, when the infinite domain is truncated by a fictitious boundary, which encloses the area of interest (usually, a circle or a sphere of radius R, large enough in comparison with the characteristic size of the system, a). Then the asymptotic behaviour of the solution is converted into the so-called Absorbing Boundary Condition (ABC) [7] on the fictitious boundary. Accuracy of the ABCs depends on the frequency and the size of the truncation domain (ratio R/a). In this work, we are interested in the performance of isogeometric collocation. Therefore in all numerical examples, we excluded the boundary truncation error on the fictitious boundary by prescribing Robin boundary condition with the right-hand side derived from the exact analytical solution in the unbounded domain.

1.1. Isogeometric analysis: Galerkin (IGAFEM) and Collocation (IGA-C)

While Finite Element Method (FEM) remains the most commonly used numerical method in engineering applications, isogeometric analysis (IGA) has gathered a considerable amount of attention in the computational mechanics community over the last decade. IGA was proposed by Hughes et al. [8,9] as a next generation of FEM (IGAFEM), that aims to conciliate the gap between the Computer-Aided Design (CAD) model and the numerical analysis. With the main idea of preserving the original geometry, usually given by a Non-Uniform Rational B-Spline (NURBS) parameterization, the NURBS basis function are used instead of Lagrange polynomials from the FEM discretization. IGA has been successfully implemented in several fields, such as structural mechanics [10], shape optimization [11–13], fluid–structure interaction [14,15], shell analysis [16–18], vibrations [19–21], fracture mechanics [22–24], electromagnetic [25,26], Helmholtz equation [27–29], among others. A complete review of IGA and its different implementation aspects can be found in [30,31].

IGA is widely used in the framework of the boundary element method (IGABEM), particularly in time-harmonics acoustics [32]. Due to the fact that the Green's function satisfies the Sommerfeld radiation condition exactly, boundary value problems in unbounded domains can be reduced to boundary integral equations on the inner boundaries without the need to truncate the domain and introduce a boundary truncation error [33]. Note, that in BEM, governing integral equations can be solved in the Galerkin framework or imposed at a set of points, an approach known as collocation. In the BEM, C^0-continuous shape functions could be sufficient for collocation. However, in the context of partial differential equations, global continuity of shape functions has a significant effect on convergence and stability of collocation. NURBS and other types of splines possess features of degree elevation with assuring desired global continuity within a patch, which makes them attractive for the so-called isogeometric collocation (IGA-C).

IGA-C was initially proposed by Auricchio et al. [34,35]. Lin et al. [36] studied the consistency and convergence properties of IGA-C for the 1-D formulation, while Schillinger et al. [37] compared isogeometric collocation with both Lagrange FEM and IGAFEM formulation, showing that while IGAFEM outperforms IGA-C in terms of accuracy per DOF, IGA-C is more efficient than IGAFEM in terms of accuracy per unit of computational time.

IGA-C has been employed in various applications, such as two-dimensional elastostatic and explicit dynamic problems [35], Timoshenko beams [38] and rods [39], Bernoulli–Euler beams and Kirchhoff–Love plates [40], and Reissner–Mindlin plates [41]. Moreover, De Lorenzis et al. [42] proposed a hybrid collocation-Galerkin formulation to treat Neumann and contact boundary conditions.

A topic of particular interest in the IGA-C method is selection of the collocation points. The standard choice are the Greville abscissae (GA) points [43], but is well known that the convergence rate reported with Greville abscissae is sub-optimal, i.e. of order p and $p-1$ in the L^2 error norm for odd and even degree NURBS, respectively [37].

Different studies have been performed in order to improve the convergence rate of the IGA-C. Anitescu et al. [44] studied the use of superconvergent (SC) points, leading to convergence rates of $p+1$ and p in the L^2 error norm for odd and even degrees, respectively, at the cost of solving an over-determined linear system resulting from a non-square stiffness matrix. Gomez and De Lorenzis [45] proposed a set of collocation points that are related to the Galerkin solution of the system, which in general is unknown. A numerical approximation of these points is in

fact a subset of the superconvergent points from [44], achieving convergence rates of p in the L^2 error norm for both even and odd degrees. In this work, we will refer to the collocation points from [45] as *Approximated Cauchy Galerkin (AGC)* points. Montardini et al. [46] proposed a different choice of subset of superconvergent points from [44] (called clustered superconvergent points (C-CSP), which correspond to two symmetric superconvergent points from [44] in every other element). This choice also leads to the same convergence rate as in [44] but avoids having more equations than the degrees of freedom. Note, that for even p, the collocation points from [45] and [46] coincide.

1.2. Partition of unity and generalized methods

In acoustics and wave propagation analysis, the error of the numerical solution consists of the discretization error and the pollution error (see a detailed discussion in [47]), and as the wave number k grows, the pollution error becomes dominant.

One approach to reduce the pollution error is to employ High-order FEM. High-order FE formulations applied to the Helmholtz equation [48–51] have proved to be more accurate and effective in coping with the pollution error than low order methods, but at the expenses of increasing condition numbers and higher computation cost when the degree p increases.

Other approach to overcome the pollution error consists in modifying the basis functions in such a way that captures the highly oscillatory behaviour of the solutions.

The Partition of Unity (PU) enrichment, initially proposed by Melenk and Babuška [52,53], consists in enhancing the original set of basis functions with a new set, derived from *a priori* knowledge of the main features of the governing partial differential equation and its analytical solution. In the case of the Helmholtz equation, the general solution takes the form of either the Bessel functions or plane waves. The results of these initial studies show that the PU enrichment of FEM has advantages in terms of the error vs the number of Degrees of freedom (DOFs) in comparison with standard FEM. In these early studies, certain drawbacks of the PUFEM, such as high condition number of the stiffness matrix, were also documented. A detailed analysis of the performance of the PUFEM in terms of the condition number, geometry description and presence of multiple scatters is given in [54].

Subsequently, the Generalized Finite element method (GFEM) [55,56] was proposed. GFEM, PUFEM and XFEM refer to the same idea of enrichment and are often used interchangeably. However, some authors distinguish GFEM as the method that employs solution approximation consisting of both, the original and enriched bases, contrary to PUFEM, which only uses the enriched basis. The data in the literature show that the GFEM and PUFEM produce similar results in the context of the Helmholtz equation, namely, advantages in terms of the error vs the number of DOFs at the price of high condition number are reported. The optimal relation between the mesh size, degree of polynomial shape function and number of plane-wave functions is still an open question. A review of different enrichment methods applied to the Helmholtz equation can be found in [57].

Different choices of enrichment applied to the Helmholtz equation are available, such as the plane-wave functions, wave-band functions and the Generalized Harmonic Polynomial. For instance, Strouboulis et al. [56] studied the effect of the enrichment set employed in the GFEM applied to Helmholtz equation, showing that all of them deliver similar results in terms of error norm versus DOFs and that the selection of the local bases should thus be determined by other factors such as the ease of the implementation or the computational cost.

Those enriched formulations have been also implemented in conjunction with the BEM [58], IGABEM [59,60] and IGAFEM [61,62] (also refereed as eXtended BEM (X-BEM), eXtended IGABEM (X-IGABEM) and Partition of Unity IGAFEM (PUIGA) respectively), showing in all cases certain improvements over the non-enriched methods.

One particular drawback that enriched formulations have is related to numerical integration of the enriched functions. Enriched formulations require the numerical integration of highly oscillatory functions, which is usually done using high-order Gauss quadrature. Still, as it has been reported by [63,64], using high-order Gauss quadrature does not deliver accurate results for high wave numbers. For instance, Banerjee and Sukumar [64] proposed an exact integration scheme for linear plane-wave enriched FEM that delivers exact integration, and it is independent of the wave number.

Note, that in the case of the Helmholtz equation, the enrichment is applied globally. In other applications, such as for example, problems with fracture and inclusions, the enrichment of the solution is used only in the vicinity

of the area of interest, i.e. X-FEM [65], X-BEM [58], and their isogeometric versions, as developed for example in X-IGAFEM [66], X-IGABEM [67]. Other wave-related areas, such as time-dependent problems of electromagnetic wave [68] and 3D elastic wave modelling [69], have been studied under the PUFEM formulation.

To the authors' knowledge, no articles are available which combine the IGA-C and the enrichment for the Helmholtz equation.

1.3. Contribution

In this work, we pair the isogeometric collocation (IGA-C) with the Generalized enrichment of two types, plane waves and harmonic functions, to solve 2D-problems for the Helmholtz equation. We conduct a parametric study and provide a detailed assessment of the performance of the method in a number of benchmark problems. We investigate the influence of the number of shape functions in the original and enriched basis and number and location of collocation points on the convergence rate and the condition number of the stiffness matrix.

The numerical results for the IGA-C and the enriched IGA-C are obtained under the formulation of the Geometry Independent Field approximaTion (GIFT) [70]. In our formulation, both the geometry and the field basis are given by NURBS, but we keep the geometry unchanged, while $h-$ and $p-$ refinement is only applied to the field basis.

1.4. Outline of the paper

The outline of the paper is as follows: The mathematical formulation of the Helmholtz equation is given in Section 2. Section 3 is devoted to NURBS, the theoretical framework of collocation method and description of the collocation schemes, while Section 4 deals with enriched formulations for the Helmholtz equation in the context of isogeometric collocation. Numerical examples are presented in Section 5, while the main results are summarized in Section 6.

2. Exterior time harmonic acoustic wave propagation

The general acoustic problem in domain Ω with boundary $\Gamma = \partial\Omega$ (see Fig. 1) can be stated as
Find u such that

$$\Delta u + k^2 u = 0 \qquad \text{in } \Omega \tag{2}$$

$$u = g, \qquad \text{on } \Gamma_D \tag{3}$$

$$\nabla u \cdot \mathrm{n} = h \qquad \text{on } \Gamma_N \tag{4}$$

$$\frac{\partial u}{\partial n} - \mathrm{i}ku = f \qquad \text{on } \Gamma_R, \tag{5}$$

where g, h, f are the prescribed Dirichlet, Neumann and Robin boundary conditions on their corresponding parts of the boundary, i.e. Γ_D, Γ_N and Γ_R respectively. Note, that $\Gamma_D \bigcup \Gamma_N \bigcup \Gamma_R = \Gamma$ and $\Gamma_D \bigcap \Gamma_N \bigcap \Gamma_R = \emptyset$.

3. Isogeometric Collocation

3.1. Non-Uniform Rational B-splines (NURBS)

A knot vector is a set of non-decreasing real numbers that represent the coordinates in the parametric space, i.e.

$$\Xi = \left\{\xi_1, \xi_2, \ldots, \xi_{n+p+1}\right\}, \tag{6}$$

where p is the order of the spline and n is the number of basis functions.

B-splines basis functions for $p = 0$ are defined as piecewise constants:

$$N_{i,0}(\xi) = \begin{cases} 1, & \text{if } \xi_i \leq \xi < \xi_{i+1} \\ 0, & \text{otherwise} \end{cases} \tag{7}$$

then, for $p \geq 1$ B-splines are defined recursively by the following formula

$$N_{i,p}(\xi) = \frac{\xi - \xi_i}{\xi_{i+p} - \xi_i} N_{i,p-1}(\xi) + \frac{\xi_{+p+1} - \xi}{\xi_{i+p+1} - \xi_{i+1}} N_{i+1,p-1}(\xi), \tag{8}$$

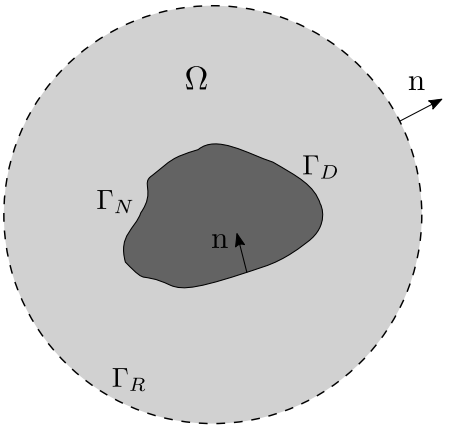

Fig. 1. Schematic of a general acoustic problem. Ω represents the problem domain, Γ_D, Γ_N and Γ_R are the Dirichlet, Neumann and Robin boundaries respectively. **n** denotes the normal vector, outer to Ω.

Non-Uniform Rational B-splines (NURBS) are subsequently defined as

$$R_i^p(\xi) = \frac{N_{i,p}(\xi) w_i}{\sum_{\hat{i}=1}^{n} N_{\hat{i},p}(\xi) w_{\hat{i}}}, \tag{9}$$

where w_i is the weight corresponding to the $i-$th B-spline function.

In 2D, NURBS are defined as the tensor product between two one-dimensional NURBS, i.e.

$$R_{i,j}^{p,q}(\xi, \eta) = \frac{N_{i,p}(\xi) M_{j,q}(\eta) w_{i,j}}{\sum_{\hat{i}=1}^{n} \sum_{\hat{j}=1}^{m} N_{\hat{i},p}(\xi) M_{\hat{j},q}(\eta) w_{\hat{i},\hat{j}}}, \tag{10}$$

where the second set of B-splines $M_{j,q}(\eta)$ of degree q is defined on knot vector $\Xi_2 = \left\{\eta_1, \eta_2, \ldots, \eta_{m+q+1}\right\}$ (with m being the number of basis functions $M_{j,q}(\eta)$).

The mapping between the parametric space $\hat{\Omega} = [\xi_1, \xi_{n+p+1}] \times [\eta_1, \eta_{m+q+1}]$ and the physical space Ω is given by

$$\mathbf{F}(\xi, \eta) = \sum_{i=1}^{n} \sum_{j=1}^{m} R_{i,j}^{p,q}(\xi, \eta) \mathbf{B}_{i,j} = [x, y]^T, \tag{11}$$

where $\mathbf{B}_{i,j}$ are the control points defined in the physical space. In what follows we use the following notation

$$R_I(\xi, \eta) = R_{i,j}^{p,q}(\xi, \eta) \tag{12}$$

with multi-index I, that combines (i, j) and takes values $I = 1, \ldots, n \times m$.

For computational details regarding B-splines and NURBS, the reader is referred to [71].

3.2. Collocation method

We consider the strong form of a boundary value problem, which is written as

$$\mathscr{L} u = f, \qquad \text{in } \Omega \tag{13}$$

$$\mathscr{G} u = g, \qquad \text{on } \Gamma \tag{14}$$

where $\mathscr{L} u = \Delta u + k^2 u$, and $\mathscr{G} u$ corresponds to a combination of Dirichlet, Neumann and Robin boundary conditions. The solution u^h is approximated as

$$u^h(x, y) = \sum_{I=1}^{n \times m} \phi_I \left(R_I \circ \mathbf{F}^{-1}\right)(x, y), \tag{15}$$

Table 1
Location of superconvergent points [44] for the second derivative on a reference element $[-1, 1]$.

Degree	SC points - second derivative
$p = 2$	0
$p = 3$	$\pm 1/\sqrt{3}$
$p = 4$	$-1, 0, 1$
$p = 5$	$\pm\sqrt{225 - 30\sqrt{30}}/15$
$p = 6$	$-1, 0, 1$
$p = 7$	± 0.5049185675126533

where ϕ_I are unknown control variables , and $R_I \circ \mathbf{F}^{-1}$ denotes a function composition between the inverse mapping of the geometry $\mathbf{F}^{-1}$, and the NURBS basis functions R_I.

The main idea of collocation is to select a set of points $\boldsymbol{\alpha}_J \in \Omega \cup \Gamma$, where the differential equation and the boundary conditions are satisfied by an approximate solution u^h. In IGA-C, collocation points are first defined in the parametric space ($\hat{\boldsymbol{\alpha}}_J \in \hat{\Omega}$) and then mapped to physical space by

$$\boldsymbol{\alpha}_J = \mathbf{F}(\hat{\boldsymbol{\alpha}}_J). \tag{16}$$

Therefore, the collocation solution u^h is required to satisfy:

$$\mathscr{L}u^h(\boldsymbol{\alpha}_J) = f(\boldsymbol{\alpha}_J), \qquad \text{in } \Omega \tag{17}$$

$$\mathscr{G}u^h(\boldsymbol{\alpha}_J) = g(\boldsymbol{\alpha}_J), \qquad \text{on } \Gamma \tag{18}$$

Eqs. (17) and (18) are subsequently converted into a linear system

$$\boldsymbol{M}\boldsymbol{X} = \boldsymbol{F}, \tag{19}$$

which is solved for the vector of unknown control variables $\boldsymbol{X} = \{\phi_1, \phi_2, \ldots, \phi_{n\times m}\}$.

3.3. Collocation points and superconvergent points

The choice of the collocation points is fundamental to ensure the convergence of the IGA-C. The most common choice is the Greville abscissae points $\hat{\alpha}_{GA}$, which are computed based on the knot vector. The formula for the Greville abscissae (GA points) points for a NURBS curve is given by [43]

$$\hat{\alpha}_{GA_i} = \frac{1}{p}\sum_{j=i}^{i+p+1} \xi_i, \tag{20}$$

where p is the degree of the B-spline and ξ_i are the knots.

The GA points lead to convergence rates of $p - 1$ and p for odd and even degrees of B-splines, respectively, in the L^2 error norm. Despite the sub-optimal convergence rate, GA points are the most popular choice of collocation points in the literature on IGA-C.

Various studies aimed to improve the convergence rate of the IGA-C method. For instance, Anitescu et al. [44] proposed the use of the superconvergent points (SC points). Superconvergent points arise from the works of Zienkiewicz and Zhu [72,73], based on the idea that, in the context of FEM, there exist some points x^* in domain Ω in which the numerical solution u_h is more accurate in comparison with any other set of points in Ω. Following the same idea, in [44] these superconvergent points were computed for B-splines of C^{p-1} continuity in a reference element $[-1, 1]$ and subsequently mapped to each knot span (Table 1). These superconvergent points lead to convergence rates of $p + 1$ and p for odd and even B-splines degrees in the L^2 error norm. However, the main drawback of the method is that the number of SC points exceeds the number of DOFs. Therefore this formulation leads to a non-square system of equations that must be solved in the least-square sense. As we show in our numerical examples, this is particularly detrimental to the precision of the IGA-C approach and its ability to overcome the pollution error.

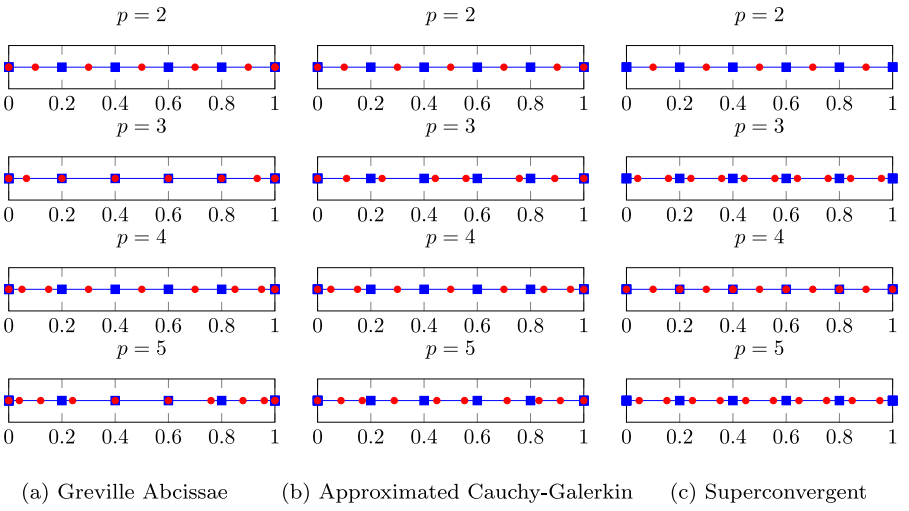

(a) Greville Abcissae (b) Approximated Cauchy-Galerkin (c) Superconvergent

Fig. 2. Collocation points and knot vector: Distribution of (A) Greville Abcissae, (B) Approximated Cauchy-Galerkin and (C) Superconvergent points for B-splines of degree $p = 2, \ldots, 5$ using five elements. The blue squares represent the position of the knots and the red points represent the collocation points.

As shown in Gomez and De Lorenzis [45], there exists a set of collocation points that produces exactly the Galerkin solution when they are evaluated in Eq. (15). These points $\boldsymbol{\tau}_j$ are called Cauchy-Galerkin points (CG points), and they depend on the unknown solution. In their work, Gomez and De Lorenzis derived a numerical approximation of these points that coincides with the SC points proposed by Anitescu et al. [44], and selected a subset of these points that matches the number of B-splines basis functions and contains at least one point per basis support (referred as Approximated Cauchy-Galerkin (ACG) points in this work). ACG points deliver a convergence rate of p for both odd and even B-splines in the L^2 error norm. The main advantage of the ACG set of collocation points is that it improves the convergence rate compared to the GA set while keeping a ratio one to one with the number of collocation points and the number of control points (or DOFs), which makes the solving process faster and less expensive. See Listing 1 in [45] for a Matlab® code that produces the ACG points.

Fig. 2 shows the position of the different collocation point sets discusses for B-splines of degree $p = 2, 3, 4, 5$ using open knots vector of five elements.

In this work, GA , SC and ACG collocation points have been tested for both the IGA-C and the enriched IGA-C methods. As we will discuss in the results section, the numerical simulations show that IGA-C with SC points is superior in terms of the convergence rate, but seems to start achieving its asymptotic behaviour later than GA and ACG (in terms of DOFs), which makes it a sub-optimal choice for the Helmholtz equation with high k.

4. Enriched Isogeometric collocation for the Helmholtz equation

In Eq. (15), we stated that for a standard isogeometric collocation method, the solution is approximated as a linear combination of the NURBS basis function. In the enriched IGA-C method, a new set of basis functions is employed, which consists in a combination between the NURBS basis functions $\{R_I\}_{I=1,\ldots,n\times m}$ and a set $\left\{\Psi_j\right\}_{j=1,\ldots,q}$ of enrichment functions. Thus, the numerical solution can be approximated as

$$u^h(\xi,\eta) = \sum_{I=1}^{n\times m} R_I \phi_I + \sum_{K=1}^{n\times m}\sum_{j=1}^{q} R_K \Psi_j \psi_{Kj}, \tag{21}$$

where R_I is the standard NURBS basis function associated with the control variable ϕ_I, Ψ_j is the enrichment function, q is the total number of enrichment functions, and ψ_{Kj} are additional degrees of freedom corresponding to the enriched basis function $R_K \Psi_j$.

In this study two sets of enrichment functions are considered, namely the plane-wave (PW-) and the Generalized Harmonic Polynomial (GHP-) enrichment:

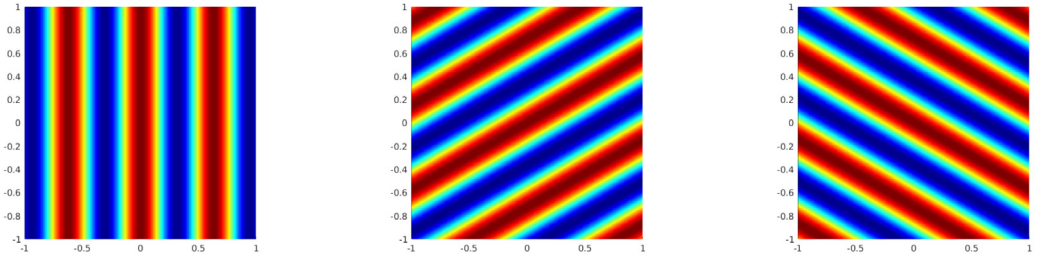

(a) $\theta_1 = 0$ (b) $\theta_2 = 2\pi/3$ (c) $\theta_3 = 4\pi/3$

Fig. 3. Real part of plane wave enrichment functions, with $q = 3$ and $k = 10$ on a $[-1, 1] \times [-1, 1]$ domain.

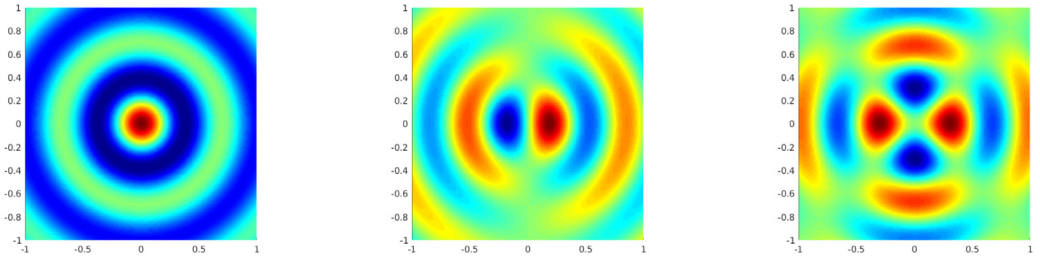

(a) $j = 0$ (b) $j = 1$ (c) $j = 2$

Fig. 4. Real part of generalized harmonic polynomial enrichment function, with $q = 3$ and $k = 10$ on a $[-1, 1] \times [-1, 1]$ domain.

4.1. Plane-Wave (PW-) enrichment

The first set of enrichment functions is a system of plane-waves that propagates in different directions. The corresponding span is given by:

$$W(q) = \text{span}\left\{\exp\left(ik\left(x\,\cos\theta_j + y\,\sin\theta_j\right)\right) \,\middle|\, \theta_j = 2\pi\frac{(j-1)}{q} + \theta_0,\, j = 1, \ldots, q\right\}, \tag{22}$$

where q is the number of propagation angles and, therefore, the number of enrichment functions and θ_0 is the starting orientation angle. For simplicity, in this study, we have considered $\theta_0 = 0$ unless otherwise stated. Fig. 3 shows an example of the real part of the plane wave enrichment functions with $q = 3$ and $k = 10$.

4.2. Generalized Harmonic Polynomial (GHP-) enrichment

The second set of enrichment functions, first presented in [55], corresponds to the Vekua functions, also known as the generalized harmonic polynomials. The corresponding span is given by:

$$V(q) = \text{span}\left\{\exp\left(\mathrm{i}j\,\theta k\right) J_j(k\,r) \,\middle|\, j = 0, \ldots, q-1\right\}, \tag{23}$$

in polar coordinates

$$\theta = \arctan\left(\frac{y}{x}\right), \quad r = \sqrt{x^2 + y^2}. \tag{24}$$

The number of enrichment functions in this case is $q = p + 1$, where p is the degree of the NURBS basis. Fig. 4 shows an example of the real part of the generalized harmonic polynomial enrichment functions with $q = 3$ ($p = 2$) and $k = 10$.

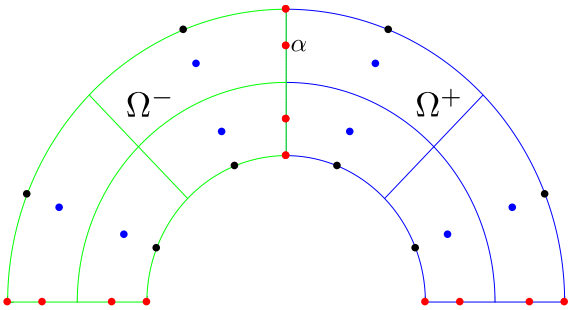

Fig. 5. Upper patches of a multi-patch mesh of a complete annulus. The blue and the green mesh represent different patches, (Ω^+) and (Ω^-) respectively, and α is a collocation point located at the interface between two patches. The red, blue and black dots represent the interface collocation points, the internal points and the external boundary points, respectively. (For interpretation of the references to colour in this figure legend, the reader is referred to the web version of this article.)

4.3. Collocation points scheme

The enriched IGA-C requires more degrees of freedom compared to the standard IGA-C. Therefore additional collocation points need to be added in order to solve the new linear equation system. It is the purpose of this paper to find a suitable way to add these additional points. The strategy that we employed in this study is to progressively add collocation points equidistantly between the original set of collocation points, and find a suitable general configuration. In Section 5.2.3, we employed a duct scattered by plane wave example in order to find the mentioned configuration.

4.4. Enriched IGA-C on multi-patch boundary problems

In the examples where multiple patches are employed, two conditions need to be satisfied on the patches interfaces in order to assure continuity of the numerical solution, namely

$$u_h|_{\Omega^+}(\alpha) = u_h|_{\Omega^-}(\alpha), \tag{25}$$

$$\left.\frac{\partial u_h}{\partial n}\right|_{\Omega^+}(\alpha) = -\left.\frac{\partial u_h}{\partial n}\right|_{\Omega^-}(\alpha), \tag{26}$$

In these equations, α is a collocation point on the interface between Ω^+ and Ω^- as shown in Fig. 5. Note, that in this study we limited attention to conforming patches, with coincident collocation points on the interfaces. A more detailed analysis regarding patch coupling in the context of IGA-C is conducted in [35].

In the case of the enriched IGA-C, generally we use more collocation points than degrees of freedom, and therefore the continuity of the solution across the patches' boundaries was enforced by including a penalty factor in Eqs. (25) and (26). The value of this penalty factor was empirically chosen as 10^6.

4.5. Linear system solvers

In the context of computational acoustics it is worth mentioning that a high number of degrees of freedom per wavelength leads to a significantly high condition number of the stiffness matrix. The numerical implementation of this method was done in Matlab. We found that direct solver was the most efficient for the matrices in this study. The matrix inversion is carried out using the backslash operator \ available in Matlab, and the condition number of a matrix is estimated by the square root of the function *condest* on $K^T K$ (also available in Matlab).

For the case of enriched IGA-C, the system of equations is non-square. Despite this, the same backslash operator from Matlab proved to be the most efficient solver available.

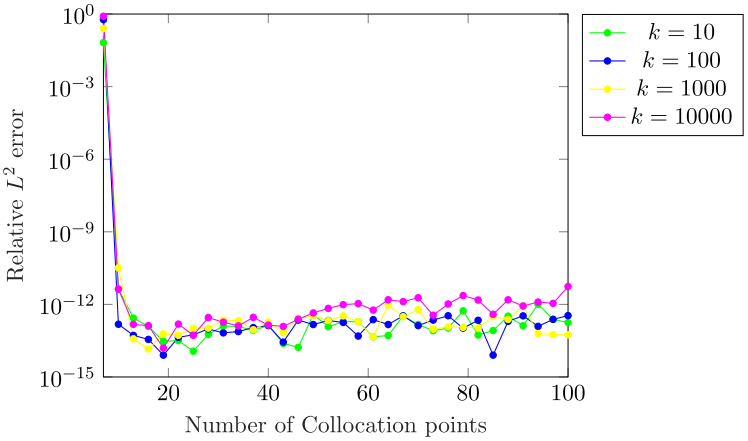

Fig. 6. One dimensional example: PW-enriched IGA-C. Relative L^2 error for $p = 3$ versus the number of collocation points for different wave number k.

5. Numerical results

In this section, we show different 1D and 2D numerical examples. For problems with known analytical solutions, we use the following relative L^2 norm of the error:

$$\frac{\|u - u^h\|_{L^2}}{\|u\|_{L^2}} = \sqrt{\frac{\int_\Omega |u - u^h|^2 \, d\Omega}{\int_\Omega |u|^2 \, d\Omega}}. \tag{27}$$

5.1. One-dimensional scattering problem

In the first example we consider a 1-Dimensional wave propagating in a space $x \in (0, 1)$, given by the following boundary value problem:

$$\begin{aligned} \frac{\partial^2 u}{\partial x^2} + k^2 u &= 0 \qquad \text{in } x \in (0, 1) \\ \frac{\partial u}{\partial x} &= ik \qquad \text{on } x = 0 \\ \frac{\partial u}{\partial x} &= -iku \qquad \text{on } x = 1 \end{aligned} \tag{28}$$

The analytical solution is given by

$$u^{\text{exact}}(x) = \exp(i\, k\, x). \tag{29}$$

The purpose of this example is to demonstrate the ability of the PW-enriched IGA-C to recover the exact solution for any value of k using the coarsest mesh (one element) and to study the influence of the number of collocation points on the accuracy of the solution. This example is analogue to the so-called patch-test in computational mechanics.

Fig. 6 shows the results of the normalized L^2 error norm versus the number of collocation points with $p = 3$ and plane-wave enrichment function ($q = 1$). One element was employed for all the simulations. The results show that plane-wave enriched IGA-C achieves machine precision for all values of k with the same optimal number of collocation points (about 19).

When using GHP-enrichment in this example, the solution is no longer exactly represented anymore, and the error depends on the mesh resolution and the number of enrichment functions. This happens because there is only one direction, and the Vekua functions are reduced to Bessel functions. The results are shown in Fig. 7. Since we are interested in the behaviour of the enrichment, a mesh of 8 elements is fixed, and the error is plotted for an increasing number of enrichment functions. It can be seen that for $q = 1, \ldots, 4$ the error decreases drastically as

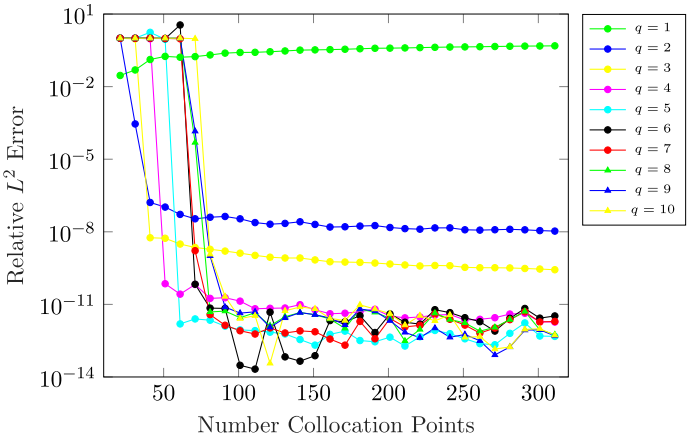

Fig. 7. One dimensional example: GHP-enriched IGA-C. Relative L^2 error for $k = 10$ and $p = 3$ versus the number of collocation points for different number of enrichment functions (q). Fixed mesh of 8 elements.

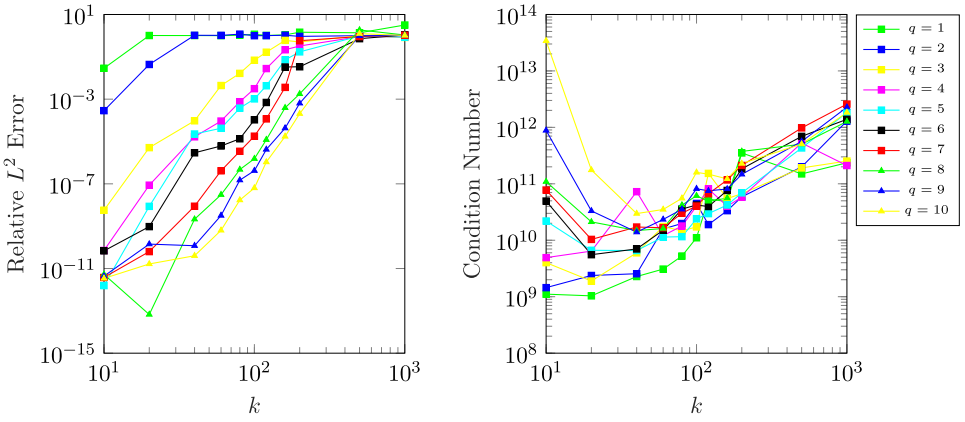

(a) Relative L^2 error norm.

(b) Condition number.

Fig. 8. One dimensional example: GHP-enriched IGA-C. Relative L^2 error norm and condition number versus wave number k for $p = 3$, fixed mesh of 8 elements and increasing q.

more enrichment functions are added. If more than four enrichment functions are added, the error still decreases but much more slowly. Note, that the error in this case significantly depends on the number of collocation points. For example, for $q = 2$ the system has 33 DOFs, but about 300 points are needed to obtain the minimum error, which cannot be improved by adding more collocation points. For $q = 7$, the optimal number of points is about 170 while the number of DOFs is 88, for $q = 10$ about 280 points with 121 DOFs, etc. This behaviour indicates that the optimal number of collocation points significantly exceeds the number of DOFs and grows with the number of enrichment functions.

In Figs. 8(a) and 8(b), the error and condition number are plotted as function of wave number k for fixed mesh and increasing q. It can be seen that the condition number grows proportionally to k but does not depend on q. An interesting observation from Fig. 8(a) is that on a fixed mesh, the efficiency of enrichment deteriorates as k grows. For example, for $k = 10$ adding 3 enrichment functions improves accuracy from 10^{-2} to 10^{-8}, i.e. by six orders of magnitude, while for $k = 100$ the same enrichment ($q = 3$) has an improvement in error from 10^{0} to 10^{-2}, and for $k = 1000$ there is no improvement in the error for q up to 10. This behaviour indicates that enrichment alone cannot be used efficiently for large k, when the pollution error dominates, and increasing the mesh resolution is also required.

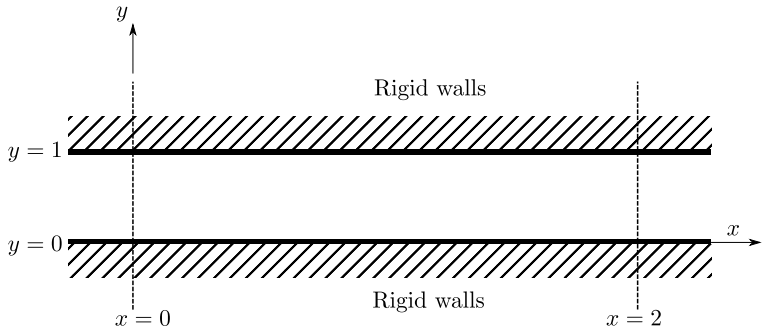

Fig. 9. The duct problem: domain.

5.2. The duct problem

In this example, we consider $\Omega = [0, 2] \times [0, 1]$ as shown in Fig. 9. We solve the following BVP:

$$\begin{aligned} \Delta u + k^2 u &= 0 && \text{in } \Omega \\ \frac{\partial u}{\partial n} &= \cos(m\pi y) && \text{on } x = 0 \\ \frac{\partial u}{\partial n} &= -iku && \text{on } x = 2 \\ \frac{\partial u}{\partial n} &= 0 && \text{on } y = 0, 1 \end{aligned} \tag{30}$$

In this problem, $m \in \mathbb{N}$ is the mode number, which is related to the Neumann boundary condition on $x = 0$. The exact solution of this problem is as follows [74]

$$u^{\text{exact}}(x, y) = \cos(m\pi y)\left(A_1 e^{-ik_x x} + A_2 e^{ik_x x}\right), \tag{31}$$

where $k_x = \sqrt{k^2 - (m\pi)^2}$ and the coefficients A_1 and A_2 are obtained from the system:

$$\begin{pmatrix} ik_x x & -ik_x \\ i\,(k - k_x)\,e^{-2ik_x} & i\,(k + k_x)\,e^{2ik_x} \end{pmatrix} \begin{pmatrix} A_1 \\ A_2 \end{pmatrix} = \begin{pmatrix} 1 \\ 0 \end{pmatrix} \tag{32}$$

If $k > m\pi$ the wave is propagating and if $k < m\pi$ the wave is evanescent. In this paper, only the propagating modes are considered and for every value of k the highest propagating mode was chosen. This means that in all the results for this example, for every value of k we picked the highest natural value of m. The only exception for this rule is $m = 0$ in Section 5.2.1 and $k = 10$, $m = 2$ in Section 5.2.2. The geometry is parameterized with linear NURBS and remains unchanged during the solution refinement process. The real and imaginary parts of the analytical solution with $k = 10$ and $m = 2$ are shown in Fig. 10.

5.2.1. Duct example: patch test for the PW-enriched IGA-C

We first start with a patch test to investigate the ability of the PW-enriched IGA-C to recover the exact solution. The exact solution is obtained from Eq. (32) with $m = 0$. In this case, two plane waves propagating in the opposite directions along x-axis can exactly represent the analytical solution. It can be seen in Figs. 11(a) and 11(b), where the relative L^2 error norm is plotted versus the number of collocation points, that for even numbers of enrichment functions nearly machine precision is achieved on one element while for odd numbers the error remains considerably large even if more enrichment functions are added. Still, the optimal number of collocation points also increases when q increases. The error seems to be independent on k (in Figs. 11(a) and 11(b), the same precision is achieved for $k = 10$ and $k = 100$), as was previously observed in the one-dimensional patch test (Section 5.1). Despite this, the result again demonstrates that the pollution error cannot be overcome by increasing the enrichment space without increasing the mesh resolution (odd q and fixed one element mesh).

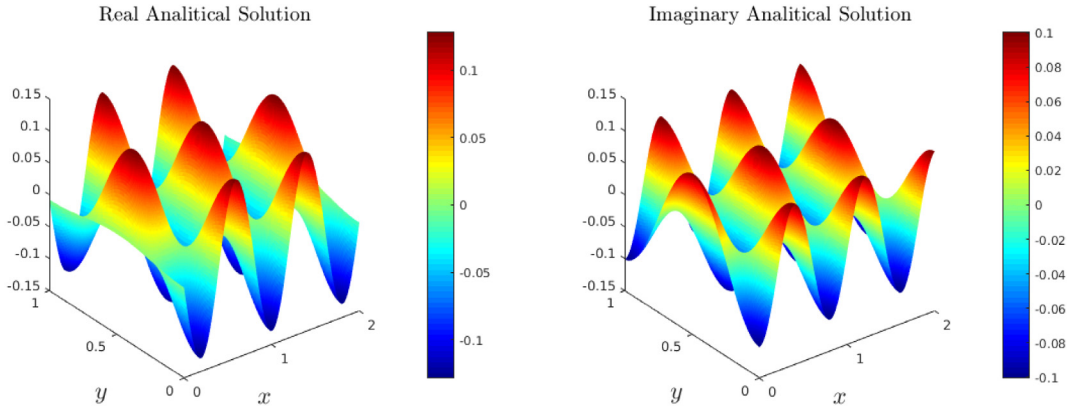

Fig. 10. Analytical solution.

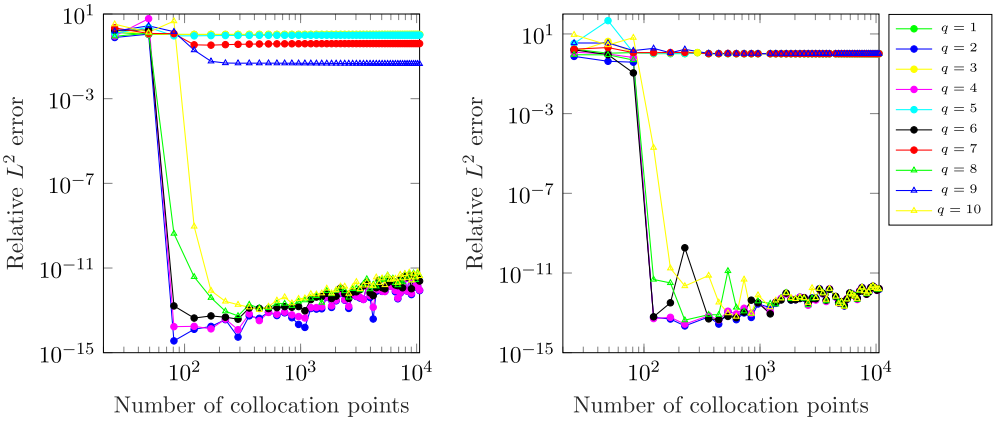

(a) $k = 10$. (b) $k = 100$.

Fig. 11. Duct patch test: PW-enriched IGA-C. Relative L^2 error for $p = 2$ versus the number of collocation points for different number of enrichment functions, $m = 0$, one element in the mesh.

5.2.2. *Convergence study for different collocation schemes*

In this study, we assess the performance of the Greville Abcissae, Approximated Cauchy-Galerkin and Superconvergent IGA-C in comparison with the Galerkin IGA. Fig. 12 shows the convergence plots in terms of the Relative L^2 error norm versus the DOFs for B-splines of degree $p = 3, 4, 5$, using $k = 10$ and $m = 2$. The plots show that IGA-C with SC points outperforms both the ACG and GA points in terms of the convergence rate. In particular, Fig. 12(b) shows that the IGA-C with ACG and IGA-C with GA lead to the same error, which is consistent with the fact that GA and ACG points for $p = 4$ are the same. The expected and observed convergences rates are summarized in Table 2. It is interesting to notice that for both even and odd p, the IGA-C with SC points delivers convergence rates slightly higher than the theoretical rates reported in the literature.

Fig. 13 shows the comparison between Greville Abcissae, Approximated Cauchy-Galerkin and Superconvergent IGA-C versus the Galerkin IGA in terms of the condition number versus the DOFs for B-splines of degree $p = 3, 4, 5$ using $k = 10$ and $m = 2$. For all the curves, the condition number increases when increasing the DOFs. Also, it can be noticed that for odd p, both the SC and the ACG collocation points leads to almost the same condition number, even though both the position and quantity of collocation points are not the same. In all the plots, the condition number reported for the Galerkin IGA is the smallest, while the condition number reported for the IGA-C with ACG points is the highest.

Fig. 14 shows the absolute error map using a fixed mesh of 4225 elements, B-splines of degree $p = 3$, and the wave parameters $k = 10$ $m = 2$ for Galerkin IGA (Fig. 14(a)) and IGA-C with SC (Fig. 14(b)), GA (Fig. 14(c))

Table 2
Duct example: Expected and observed convergence rates (L^2 error norm vs DOF) for the IGA Galerkin, IGA-C GA, SC and ACG methods from Fig. 12.

Method	Expected convergence rate	Observed convergence rate		
		$p = 3$	$p = 4$	$p = 5$
IGA Galerkin	$(p + 1)/2$	2	2.4	3
IGA-C GA	odd $(p - 1)/2$; even $p/2$	1.1	2.1	2.2
IGA-C SC	odd $(p + 1)/2$; even $p/2$	2.6	2.3	3.3
IGA-C ACG	$p/2$	1.5	2.1	2.5

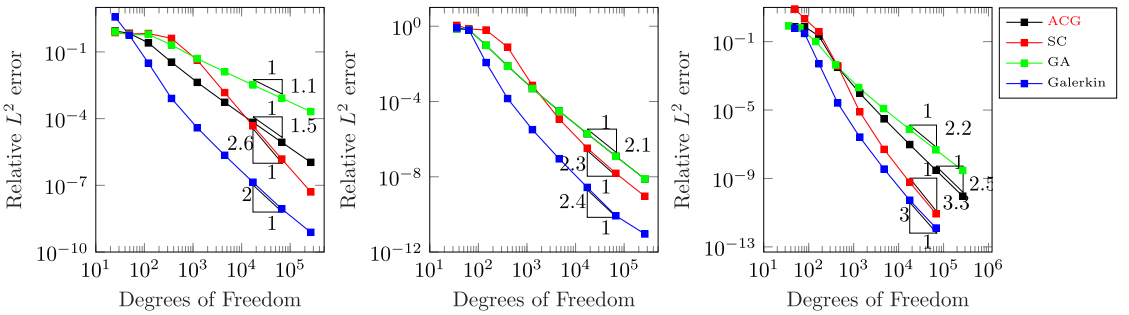

(a) $p = 3$. (b) $p = 4$. (c) $p = 5$.

Fig. 12. Duct example: Comparison between IGA-C using GA, SC and ACG points, and Galerkin IGA for the Relative L^2 error norm for B-splines of degree $p = 3, 4$ and 5, versus the number of degrees of freedom. $k = 10$ and $m = 2$.

and ACG (Fig. 14(d)) points. The absolute error map plot for the Galerkin IGA is both more symmetric and lower in terms of magnitude compared to the IGA-C methods.

Then, the wave number k is increased to 100 to study the pollution error in different methods. Figs. 15 and 16 report both the L^2 error norm and the condition number, respectively, for B-splines of degree $p = 3, 4, 5$. In this case, IGA-C for all collocation points schemes seem to be more sensitive to the pollution error in comparison with Galerkin IGA of the same degree (i.e. more DOFs are required to achieve asymptotic convergence range, and the difference between Galerkin and IGA-C error is much more significant in comparison to Fig. 12). Comparing three collocation schemes, ACG seems to perform slightly better.

As can be seen in all plots, Galerkin IGA outperforms all IGA-C schemes tested. However, the advantages of IGA-C are more evident when one considers the number of function evaluations. Fig. 17 shows the L^2 error norm versus the total number of quadrature/collocation points. For the Galerkin IGA, we employed $(p + 1)^2$ quadrature points per elements, while for the IGA-C, the number of collocation points is given by the collocation scheme. In the plots of Fig. 17, it can be seen that initially, for $p = 3, 4$, both the IGA-C with ACG and GA points are better in terms of error per collocation point, but after some 10^4 collocation/quadrature points, Galerkin IGA outperforms the other methods. For $p = 5$, it seems that IGA-C with SC and ACG points outperforms the Galerkin IGA.

For the remaining examples, IGA-C with ACG points will be employed, since it shows the best balance between the convergence rates, overall error and ratio of collocation points versus control points.

5.2.3. Collocation schemes for the enriched IGA-C

As mentioned in Section 4.3, one of the goals of this paper is to find an efficient collocation scheme for the enriched basis that we are testing. To achieve this, we started with the ACG points and progressively added additional collocation points equidistantly in between them. Figs. 18 and 19 show the convergence plots for the L^2 error norm and the condition number versus the number of collocation points, for a fixed mesh of 64 elements using PW- and GHP-enrichment, respectively. From these studies, we conclude that the most suitable choice is to add $q + 1$ and q additional equidistant collocation points between the initial ACG points, for PW- and GHP-enrichment, respectively. This number of collocation points is employed in all further studies.

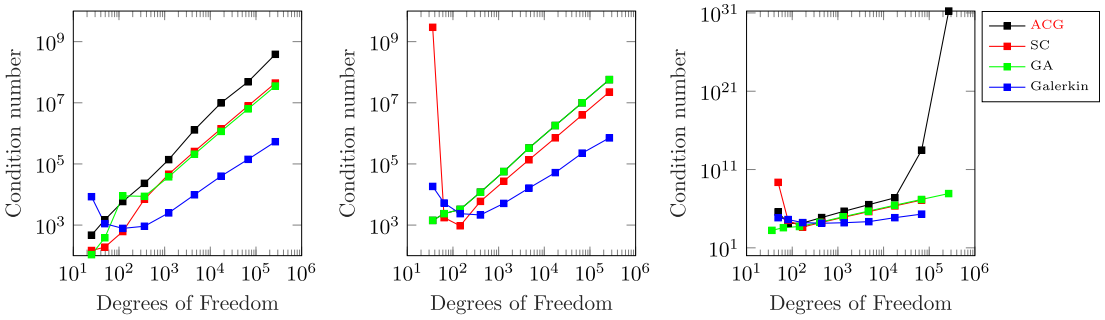

(a) $p = 3$. (b) $p = 4$. (c) $p = 5$.

Fig. 13. Duct example: Comparison between IGA-C using GA, SC and ACG points, and Galerkin IGA for the Condition number for B-splines of degree $p = 3, 4$ and 5, versus the number of degrees of freedom. $k = 10$ and $m = 2$.

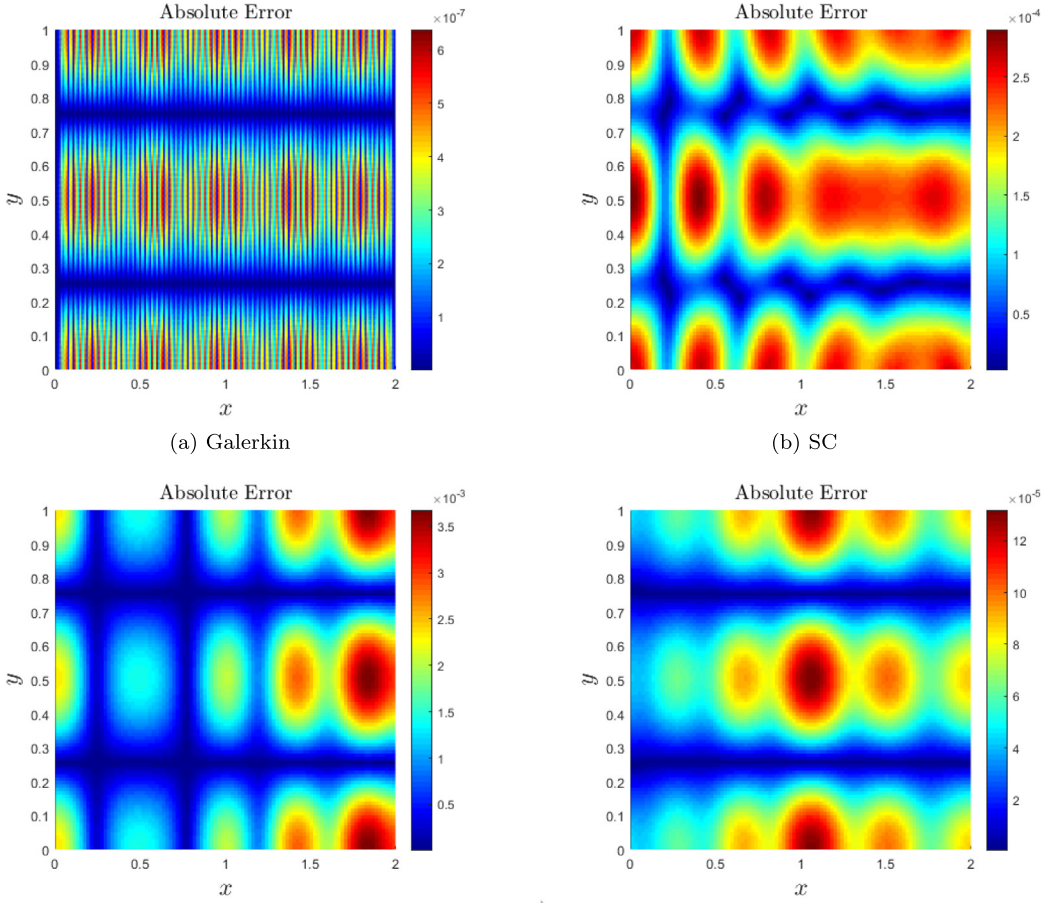

(a) Galerkin (b) SC

(c) GA (d) ACG

Fig. 14. Duct example: Absolute error for a fixed mesh of 4225 elements. Comparison between Galerkin IGA, SC, GA and ACG IGA-C methods. $p = 3$, $k = 10$ and $m = 2$.

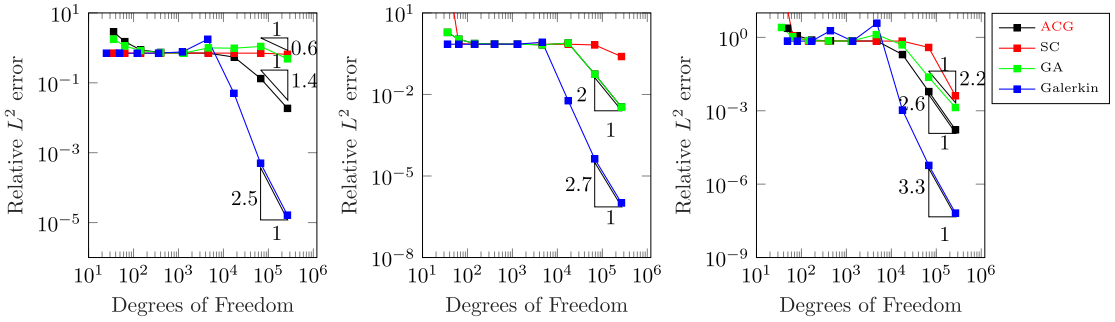

(a) $p = 3$. (b) $p = 4$. (c) $p = 5$.

Fig. 15. Duct example: Comparison between IGA-C using GA, SC and ACG points, and Galerkin IGA for the Relative L^2 error norm for B-splines of degree $p = 3, 4$ and 5, versus the number of degrees of freedom. $k = 100$ and $m = 2$.

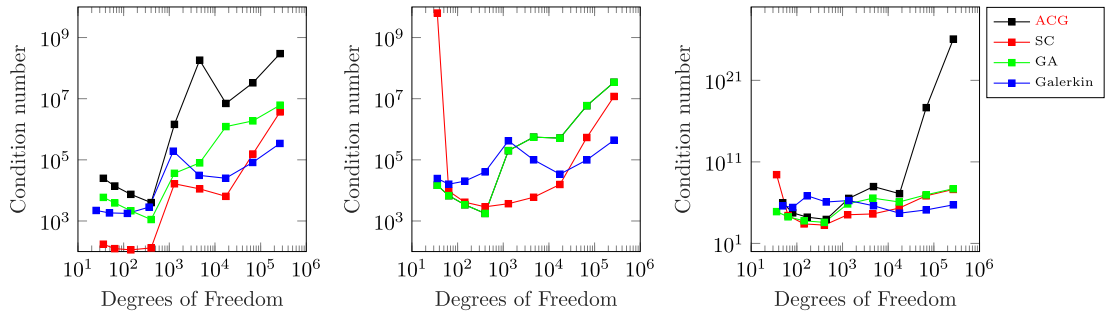

(a) $p = 3$. (b) $p = 4$. (c) $p = 5$.

Fig. 16. Duct example: Comparison between IGA-C using GA, SC and ACG points, and Galerkin IGA for the Condition number for B-splines of degree $p = 3, 4$ and 5, versus the number of degrees of freedom. $k = 100$ and $m = 2$.

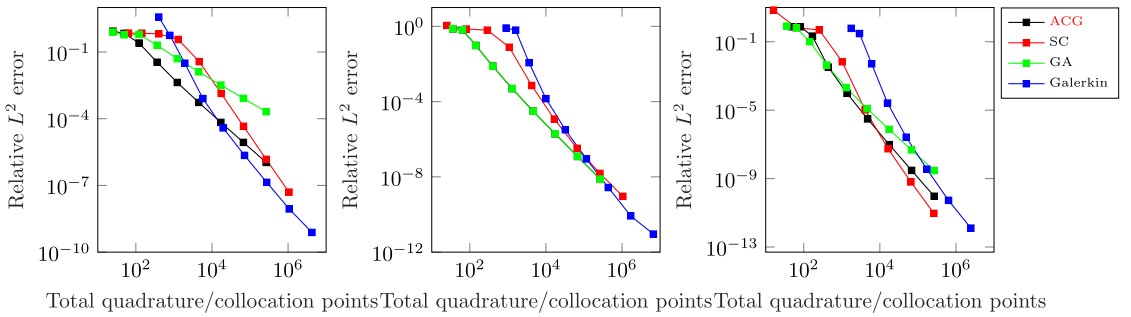

(a) $p = 3$. (b) $p = 4$. (c) $p = 5$.

Fig. 17. Duct example: Comparison between IGA-C using GA, SC and ACG points, and Galerkin IGA for the Relative L^2 error norm for B-splines of degree $p = 3, 4$ and 5, versus the number of degrees of freedom. $k = 10$ and $m = 2$.

5.2.4. PW-enrichment: convergence study for $k = 10$ and $m = 2$

Figs. 20–22 show the convergence study in terms of the DOF for both the L^2 error norm and the condition number, using $p = 3$, 4 and 5 with q from 0 to 16, $k = 10$ and $m = 2$. In all simulations PW-enrichment is employed. Note, that in this case, for any fixed q, the number of DOF is increased by $h-$refining the mesh. The

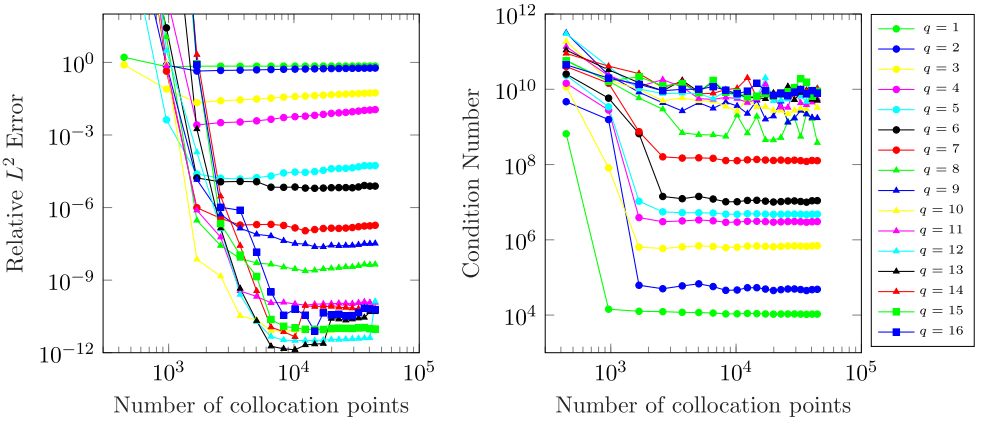

Fig. 18. Relative L^2 error and condition number using $p = 3$ and plane-wave enrichment for $k = 10$ and $m = 2$. Fixed mesh of 64 elements.

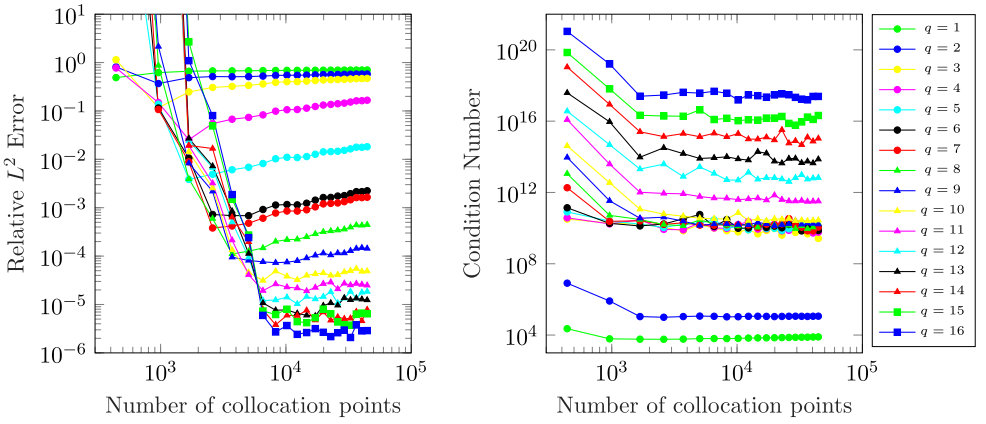

Fig. 19. Relative L^2 error and condition number using $p = 3$ and generalized harmonic polynomial enrichment (half span) for $k = 10$ and $m = 2$. Fixed mesh of 64 elements.

figures show that increasing the enrichment basis can significantly improve the overall error. However, for large numbers of enrichment function, the error seems to stay constant or even grow with h-refinement.

5.2.5. *PW-enrichment: convergence study for* $k = 120$ *and* $m = 38$

Figs. 23–25 show the convergence study in terms of the DOF for both the L^2 error norm and the condition number, using $p = 3$, 4 and 5 with q from 0 to 16. In all the simulations, plane-wave enrichment is employed. The wave number k is fixed to 120 and $m = 38$.

In this study, it can be seen that as k grows, the efficiency of enriched IGA-C deteriorates significantly. On coarse meshes, when the pollution error prevails over discretization error, no improvement in accuracy is seen even if a large number of enrichment functions are added. In the asymptotic regime, a large number of PW can improve the solution. However, the behaviour of the method is sensitive to the choice of parameters and no clear dependence between the number of PW and the accuracy of the solution is seen.

5.2.6. *PW-enrichment: wave number study*

Fig. 26 shows the convergence study in terms of the wave number for both the L^2 error norm and the condition number, using $p = 5$ with q from 0 to 16. In all the simulations, plane-wave enrichment is employed. As we mentioned at the beginning of Section 5.2, the m value for every k is chosen to be the highest natural number that allows wave propagation. The mesh is fixed to 8×8 elements. This study again shows that efficiency of

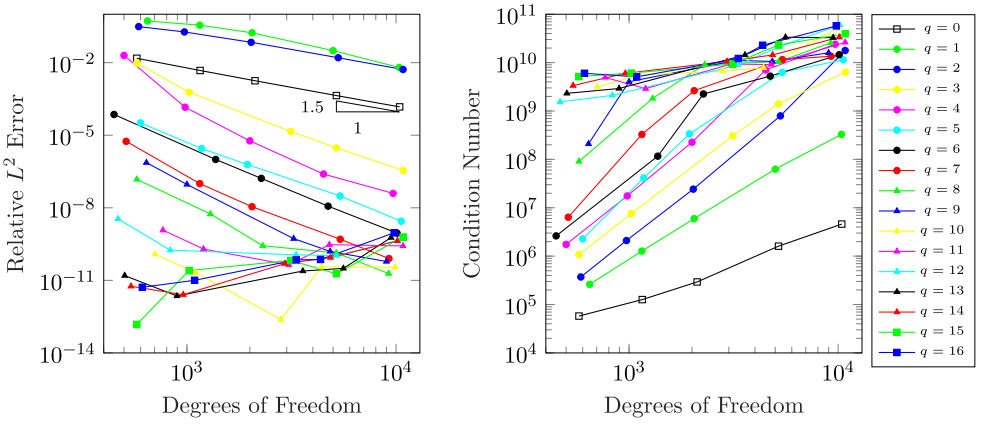

(a) Relative L^2 error norm. (b) Condition number.

Fig. 20. The duct example: Relative L^2 error norm and Condition number study for $p = 3$, $k = 10$ and $m = 2$.

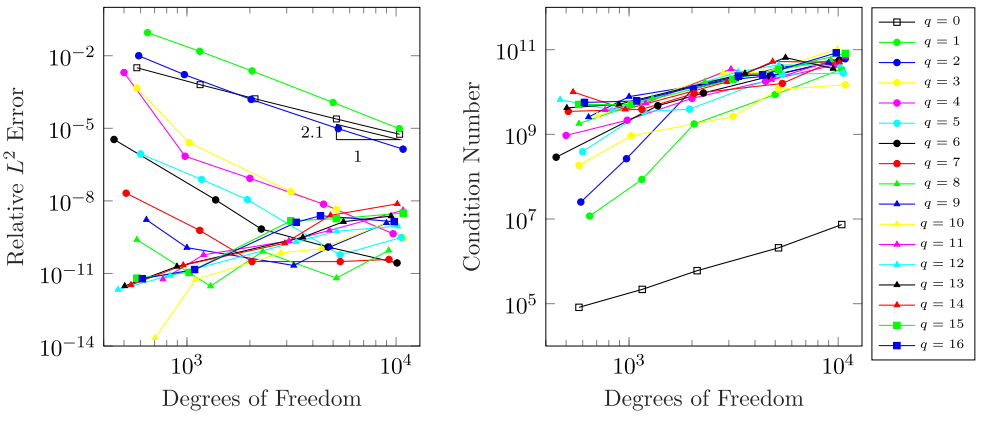

(a) Relative L^2 error norm. (b) Condition number.

Fig. 21. The duct example: Relative L^2 error norm and Condition number study for $p = 4$, $k = 10$ and $m = 2$.

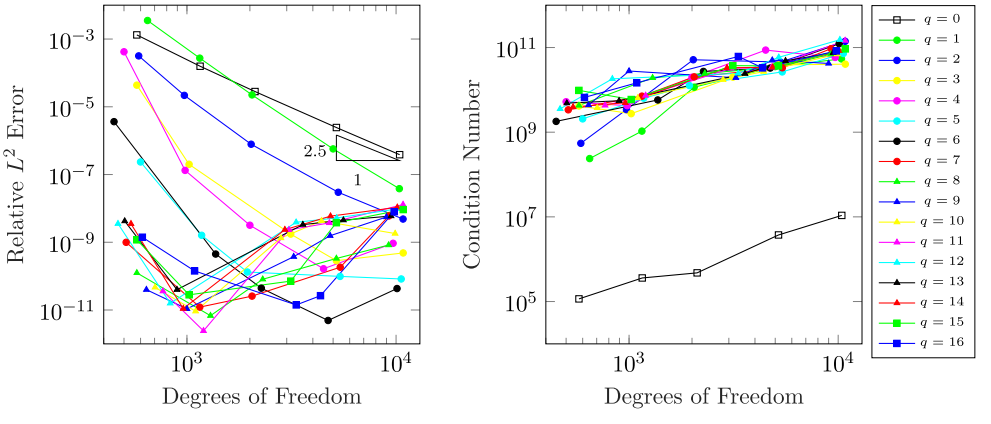

(a) Relative L^2 error norm. (b) Condition number.

Fig. 22. The duct example: Relative L^2 error norm and Condition number study for $p = 5$, $k = 10$ and $m = 2$.

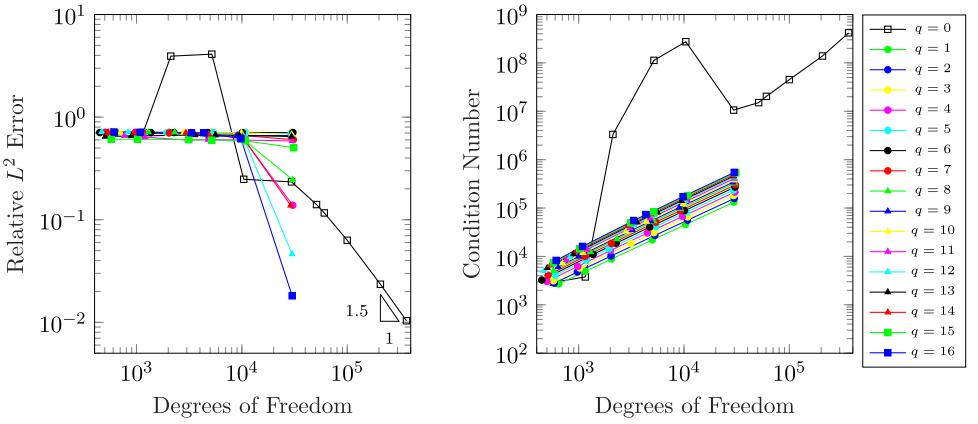

(a) Relative L^2 error norm. (b) Condition number.

Fig. 23. The duct example: Relative L^2 error norm and Condition number study for $p = 3$, $k = 120$ and $m = 38$.

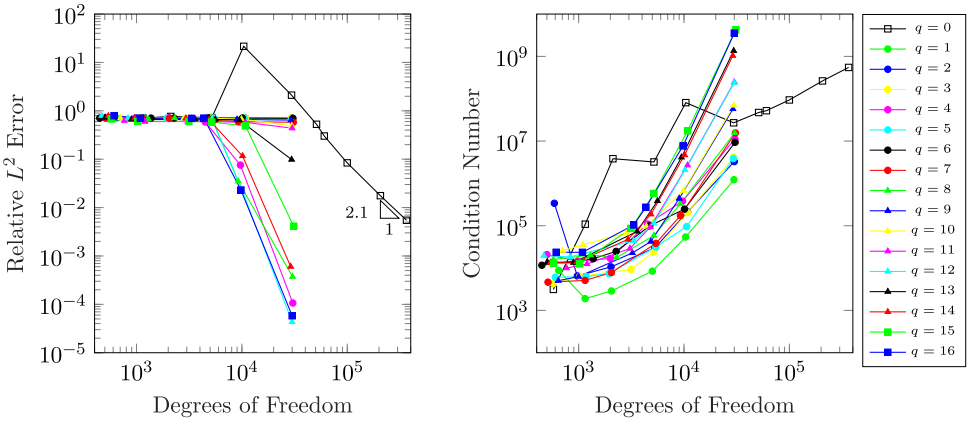

(a) Relative L^2 error norm. (b) Condition number.

Fig. 24. The duct example: Relative L^2 error norm and Condition number study for $p = 4$, $k = 120$ and $m = 38$.

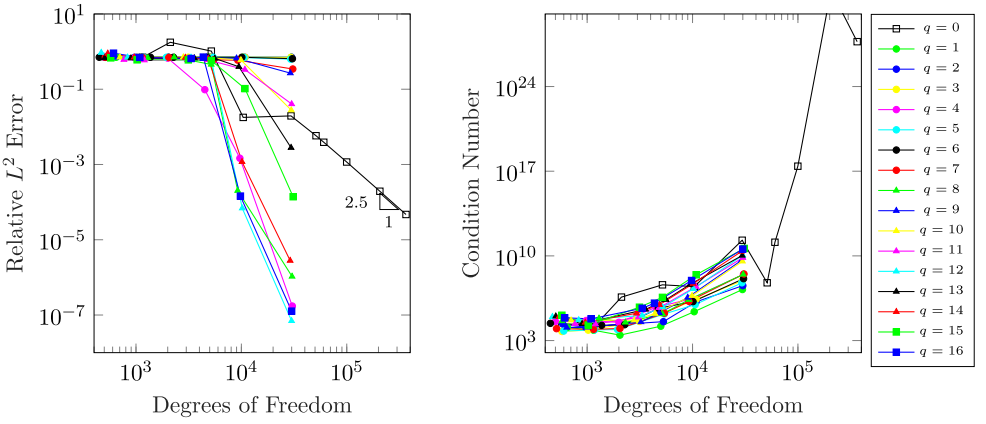

(a) Relative L^2 error norm. (b) Condition number.

Fig. 25. The duct example: Relative L^2 error norm and Condition number study for $p = 5$, $k = 120$ and $m = 38$.

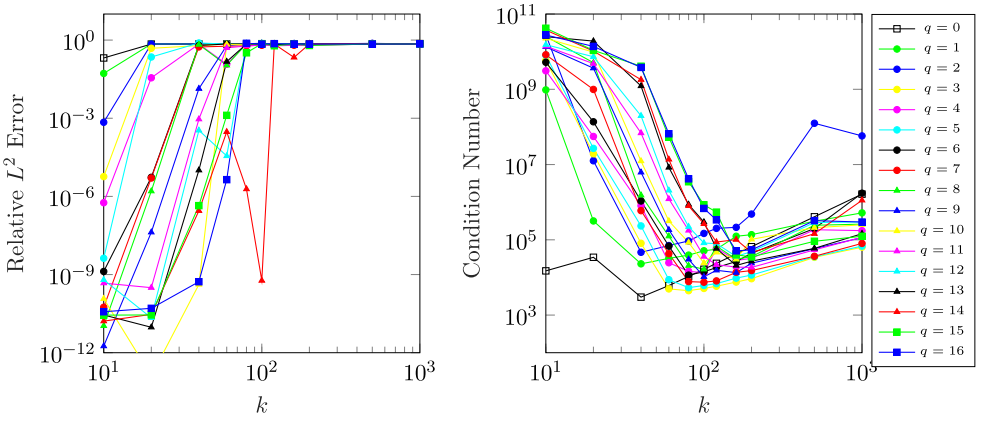

(a) Relative L^2 error norm for $p = 5$.

(b) Condition number for $p = 5$.

Fig. 26. Duct example: Wave study for a fixed mesh. Comparison between plane-wave enriched and non-enriched collocation methods. The mesh has 64 elements. $p = 5$.

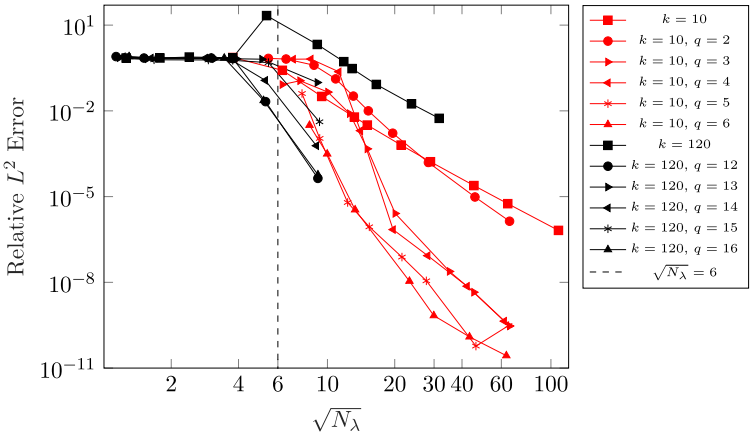

Fig. 27. Duct example: Relative L^2 error norm versus the DOF density N_λ for $k = 10$ and $k = 120$, using $p = 4$ and different numbers of enrichment functions.

PW-enrichment deteriorates as k grows, meaning that for the same accuracy, as k increases, more enrichment functions need to be added to the basis.

Finally, in Fig. 27, we show the convergence study in terms of the L^2 error norm vs. the Degree of Freedom density, i.e. the number of DOFs per wave length, $N_\lambda = \frac{4\pi^2 DOF}{k^2}$ (with $\sqrt{N_\lambda}$ being the DOF density in one direction). The results are given for $p = 4$ and $k = 10$ and 120. Both enriched and un-enriched schemes can be compared. It can be seen that for $k = 120$ and $N_\lambda \geq 6$, for the same N_λ, a large number of enrichment functions need to be added ($q \geq 12$) to see an improvement over the un-enriched scheme. For $k = 10$ improvement in the range $6 \leq N_\lambda \leq 10$ (typically used in acoustics analysis) is seen for $q \geq 5$.

5.2.7. GHP-enrichment: convergence study for $k = 10$ and $m = 2$

Figs. 28(a), 29(a) and 30(a) show the convergence study in terms of the DOF for both the L^2 error norm and the condition number, using $p = 3$, 4 and 5 with q from 0 to 16. In all the simulations, generalized harmonic polynomial enrichment is employed. The wave number k is fixed to 10 and $m = 2$. In all plots, a significant improvement between the enriched and non-enriched approach is seen. Interestingly, the error curves for $q > 5$ are close to each other, meaning that adding more enrichment functions does not improve the overall error. Another important

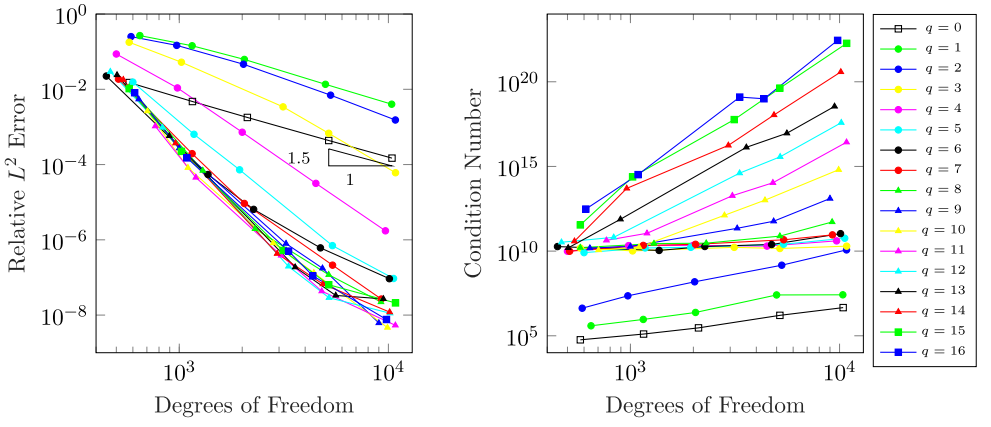

(a) Relative L^2 error norm. (b) Condition number.

Fig. 28. The duct example: Relative L^2 error norm and Condition number study for $p = 3$, $k = 10$ and $m = 2$ and varying number of GHP-enrichment functions.

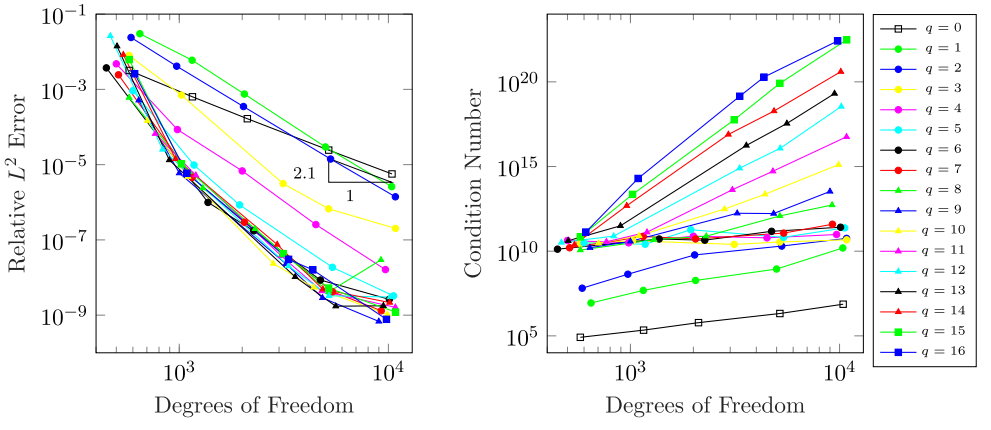

(a) Relative L^2 error norm. (b) Condition number.

Fig. 29. The duct example: Relative L^2 error norm and Condition number study for $p = 4$, $k = 10$ and $m = 2$ and varying number of GHP-enrichment functions.

observation is that the condition number for GHP-enriched IGA-C is significantly higher than the condition number in PW-enriched IGA-C, as shown in Figs. 28(b), 29(b) and 30(b).

5.2.8. GHP-enrichment: convergence study for $k = 40$ and $m = 12$

Figs. 31(a), 32(a) and 33(a) show the convergence study in terms of the DOF for both the L^2 error norm and the condition number, using $p = 3$, 4 and 5 with q from 0 to 16. In all the simulations, generalized harmonic polynomial enrichment is employed. The wave number k is fixed to 40 and $m = 12$. As it can be seen in the figures, for $k = 40$, the GHP-enrichment performs very poorly. In all three figures, the error in the non-enriched formulation is significantly lower compared to the GHP-enriched IGA-C, converging asymptotically in the entire range, while the enriched formulation requires much more degrees of freedom even to start converging.

5.2.9. GHP-enrichment: wave number study

Figs. 34(a) and 34(b) show the convergence study in terms of the wave number for both the L^2 error norm and the condition number, using $p = 5$ with q from 0 to 16. In all simulations, the generalized harmonic polynomial enrichment is employed. As before, the value chosen for m is the highest natural number that allows propagation.

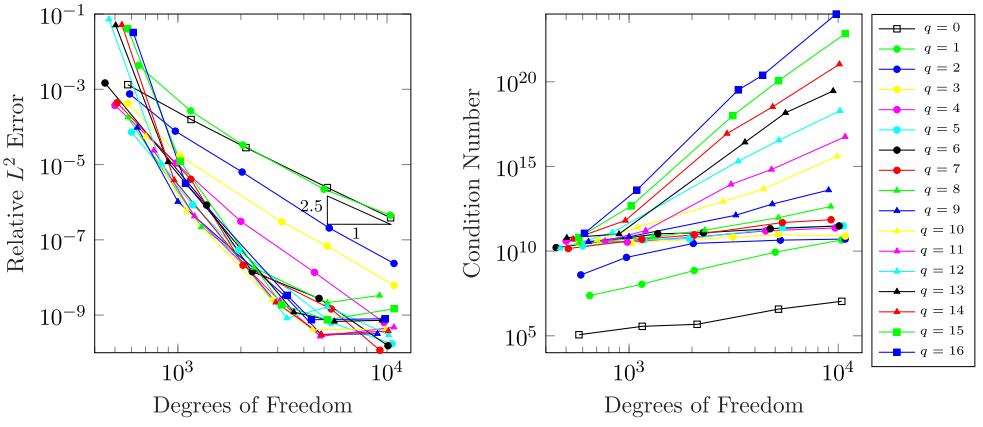

(a) Relative L^2 error norm. (b) Condition number.

Fig. 30. The duct example: Relative L^2 error norm and Condition number study for $p = 5$, $k = 10$ and $m = 2$ and varying number of GHP-enrichment functions.

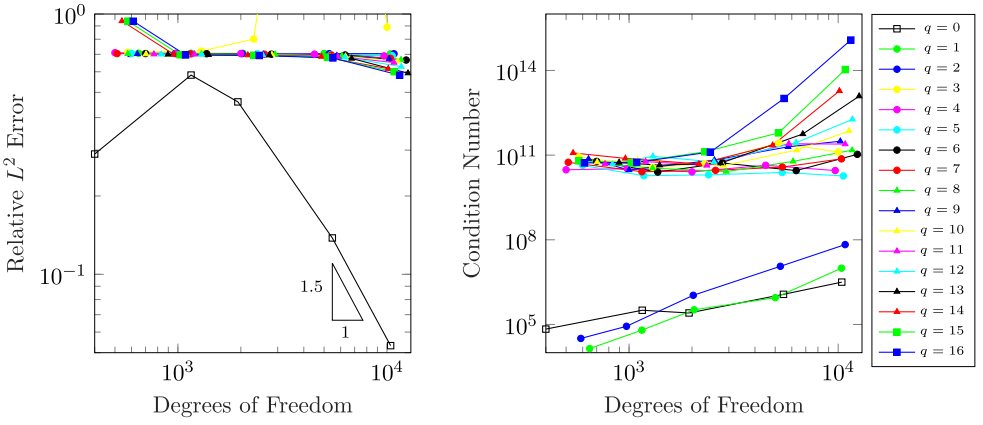

(a) Relative L^2 error norm for $p = 3$ and $k = 40$. (b) Condition number for $p = 3$ and $k = 40$.

Fig. 31. The duct example: Relative L^2 error norm and Condition number study for $p = 3$, $k = 40$ and $m = 12$, varying number of GHP-enrichment functions.

The mesh is fixed to 8×8 elements. The behaviour of GHP-enrichment is similar to PW-enrichment shown in Fig. 26. Interestingly, the range of k where GHP-enrichment improves the error is much smaller than the one in PW-enrichment, i.e. for $k > 30$ there is no improvement in the error in GHP-enriched IGA-C, even when a large number of enrichment functions is added, while in Fig. 26, the improvement in the error for PW-enriched IGA-C was observed for k up to 100. The condition number in GHP-enriched IGA-C is also higher in comparison with PW-enrichment.

5.3. Spinning wave propagation

In this example, we considered a spinning wave propagation problem. The geometry of computational domain consists of two circular cylinders of radii R_i (with boundary denoted as Γ_1) and R_e (with boundary denoted as Γ_2), centred at the origin, as shown in Fig. 35(a). The geometry consists of four NURBS patches (Fig. 35(b)) with control points given in Table A.9 from [75]. The inter-patch continuity of solution is imposed as described in Section 4.4.

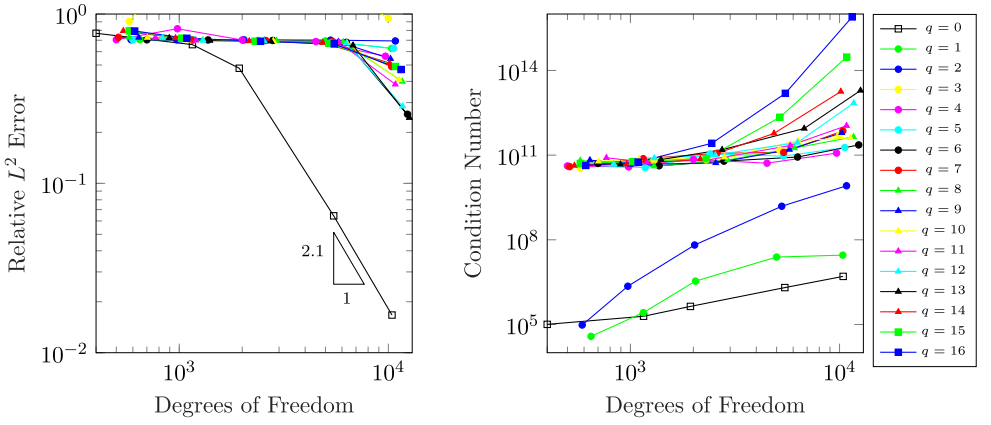

(a) Relative L^2 error norm for $p = 4$ and $k = 40$. (b) Condition number for $p = 4$ and $k = 40$.

Fig. 32. The duct example: Relative L^2 error norm and Condition number study for $p = 4$, $k = 40$ and $m = 12$, varying number of GHP-enrichment functions.

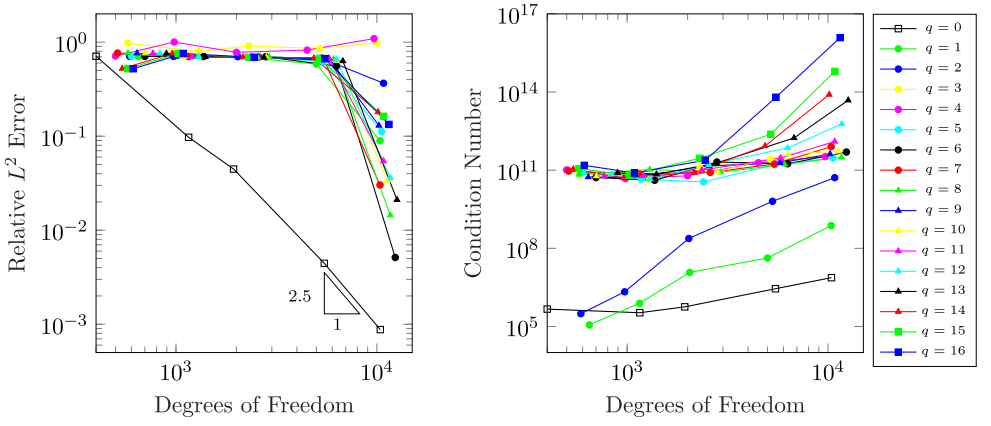

(a) Relative L^2 error norm for $p = 5$ and $k = 40$. (b) Condition number for $p = 5$ and $k = 40$.

Fig. 33. The duct example: Relative L^2 error norm and Condition number study for $p = 5$, $k = 40$ and $m = 12$, varying number of GHP-enrichment functions.

The exterior acoustic spinning wave propagation problem is stated as
Find u such that

$$\Delta u + k^2 u = 0, \qquad \text{in } \Omega \tag{33}$$

$$\frac{\partial u}{\partial n} - \mathrm{i}ku = f_1, \qquad \text{on } \Gamma_1 \tag{34}$$

$$\frac{\partial u}{\partial n} - \mathrm{i}ku = f_2, \qquad \text{on } \Gamma_2 \tag{35}$$

In the present study, we considered $R_i = 1$ and $R_e = 2$, and Robin boundary condition on both boundaries (Γ_1 and Γ_2) with functions f_1 and f_2 calculated from the analytical solution. The analytical solution is presented in [61,76],

$$u^{\text{exact}}(r, \theta) = H_m^{(2)}(kr)^{-im\theta}, \tag{36}$$

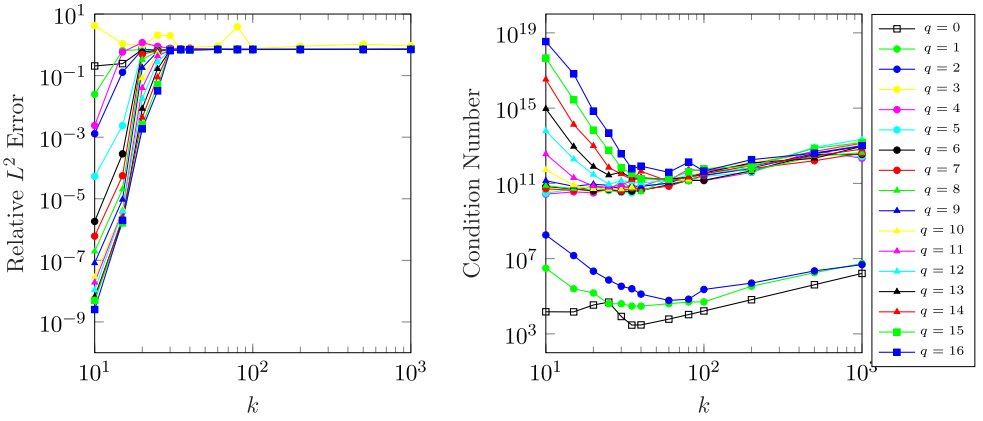

(a) Relative L^2 error norm for $p = 5$.

(b) Condition number for $p = 5$.

Fig. 34. Duct example: GHP-study for a fixed mesh. Comparison between GHP-enriched and non-enriched collocation methods. The mesh has 64 elements. $p = 5$.

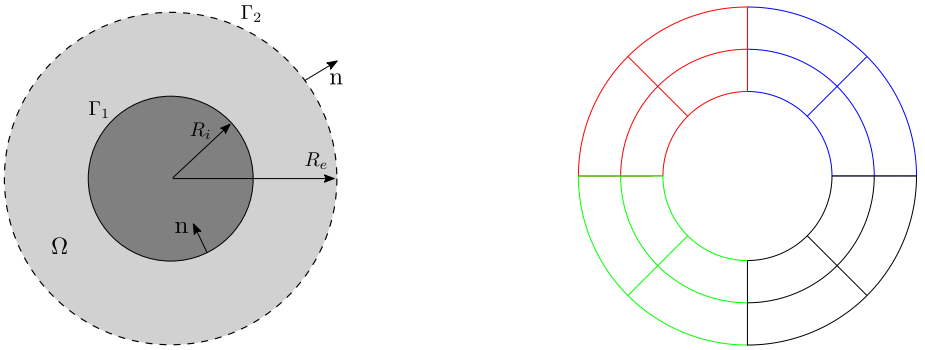

(a) Problem domain.

(b) Physical NURBS mesh.

Fig. 35. Spinning wave example: (a) Schematic of the exterior acoustic spinning wave propagation problem. Ω represents the problem domain, Γ_1 and Γ_2 are the Robin boundaries. The normal is denoted by **n**. (b) Multipatch mesh in physical space built with NURBS.

where $H_m^{(2)}$ is Hankel function of the second kind of order m, which is also the number of waves in the polar direction, and k is the wave number.

The wave will propagate with decay rate of order $1/\sqrt{r}$, where $r \in [R_i, \infty)$, if $m < kR_i$. On the other hand, if $m > kR_i$, the wave will be evanescent and it will decay with a higher rate. In this study, two wave numbers are considered, $k = 20$ and $k = 40$ with $m = 10$ and $m = 30$ for the propagating mode respectively, and $m = 22$ and $m = 42$ for the evanescent mode. The real and the imaginary parts of the solution for $k = 40$ and $m = 30$ are shown in Fig. 36.

5.3.1. Spinning wave propagation: PW-enrichment

Figs. 37 and 38 show the convergence study for both the L^2 error norm and the condition number vs DOFs, using $p = 3$ and q from 8 to 16. In all simulations, PW-enrichment is employed. In Fig. 37 the sound wave is in propagating mode since $m < kR_i$. In Fig. 38 the sound wave is evanescent. In all plots, enriched solutions show lower error in comparison with non-enriched IGA-C, but interestingly, a significant advantage of enrichment is seen only on fine meshes.

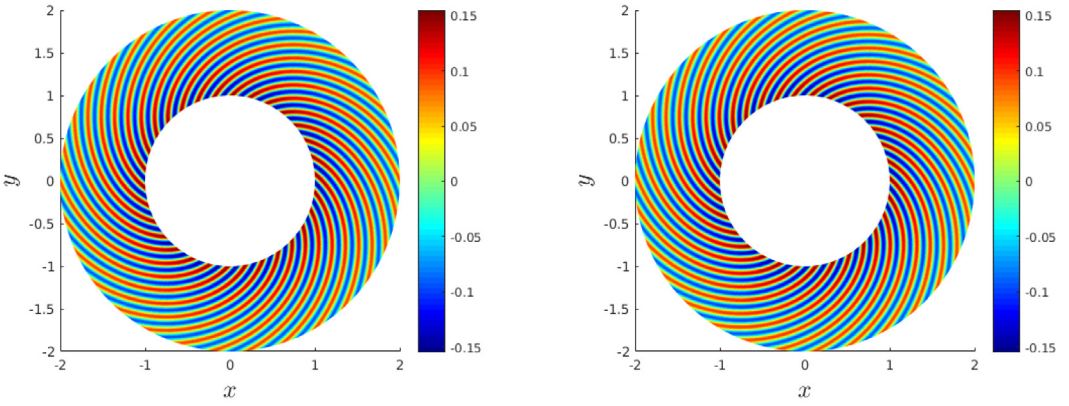

(a) Real part. (b) Imaginary part.

Fig. 36. Analytical solution of the spinning wave propagation problem with $k = 40$ and $m = 30$.

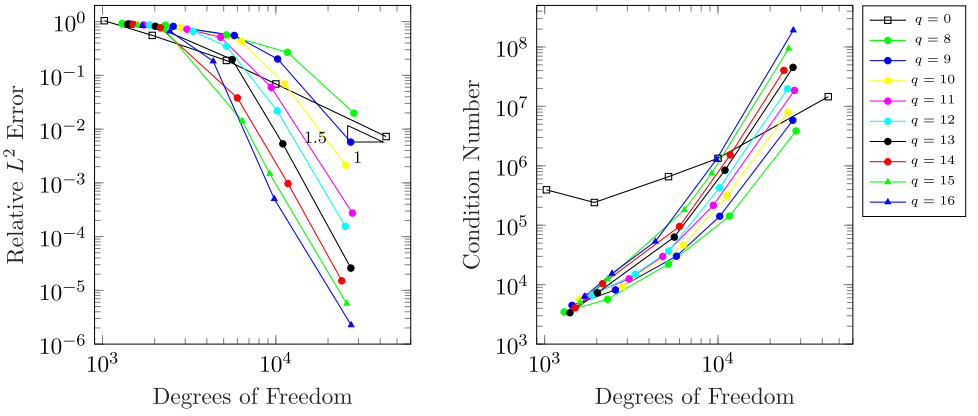

(a) Relative L^2 error. (b) Condition number.

Fig. 37. Spinning wave example: Relative L^2 error norm and condition number study for $p = 3$, $k = 40$ and $m = 30$, varying number of PW-enrichment functions.

5.3.2. Spinning wave propagation: GHP-enrichment

Figs. 39 and 40 show the convergence study in terms of the DOF for both the L^2 error norm and the condition number, using $p = 3$ and q from 8 to 16. In all simulations, the generalized harmonic polynomial enrichment is employed. In all cases, the GHP-enrichment performs quite poorly. As it is seen in the figures, the GHP-enriched IGA-C not only does not bring any improvement in the error, but it requires much more DOFs in comparison with the non-enriched IGA-C to overcome the pollution error and begin to converge. Note, that in both examples in this subsection $k = 40$, but the error of the GHP-enriched solutions for $m = 42$ is up to one order of magnitude worse than for $m = 30$.

5.4. Plane wave scattered by a cylinder

Another benchmark problem in the time-harmonic acoustic analysis is the problem corresponding to an incident harmonic plane-wave u^{inc} scattered by a sound-hard cylinder. Assuming that the incident plane-wave is travelling along the direction $\mathbf{e}_1$, it can be expressed in polar coordinates (r, θ) as

$$u^{inc}(r, \theta) = u_0 \exp(ikr \cos\theta), \tag{37}$$

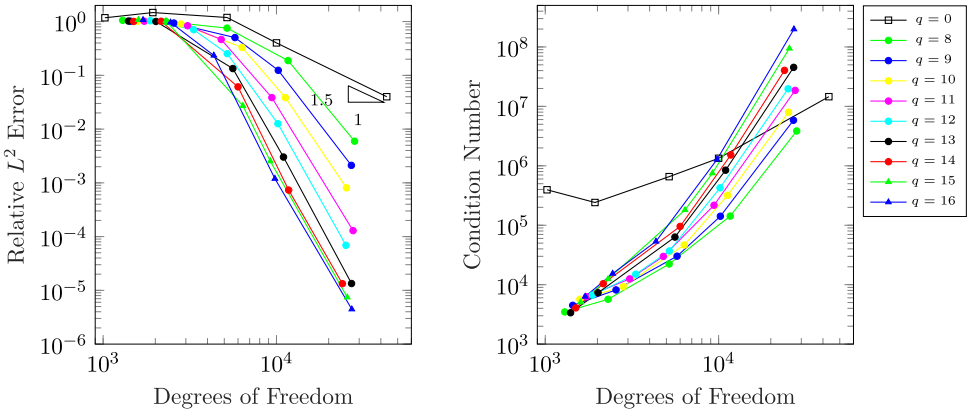

(a) Relative L^2 error. (b) Condition number.

Fig. 38. Spinning wave example: Relative L^2 error norm and condition number study for $p = 3$, $k = 40$ and $m = 42$, varying number of PW-enrichment functions.

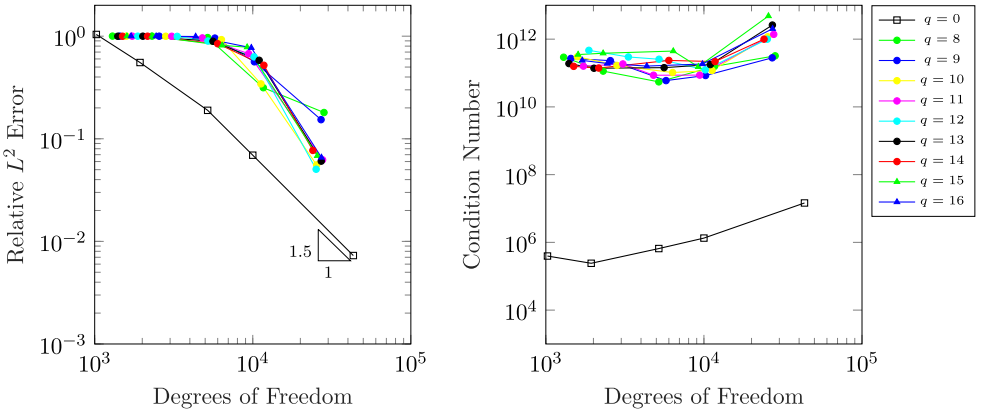

(a) Relative L^2 error. (b) Condition number.

Fig. 39. Spinning wave example: Relative L^2 error norm and condition number study for $p = 3$, $k = 40$ and $m = 30$, varying number of GHP-enrichment functions.

where u_0 is the magnitude of the wave (for simplicity, $u_0 = 1$), and k is the wave number. Then the analytical solution for the scattered wave is given by

$$u^{exact}(r,\theta) = -\sum_{n=0}^{\infty} i^n \epsilon_n \frac{J_n'(kR_i)}{H_n'(kR_i)} H_n(kr)\cos(n\theta), \tag{38}$$

where R_i is the radius of the cylinder, $H_n^{(1)}$ is the Hankel function of the first kind, J_n is the Bessel function of the first kind, k is the wave number, and the Jacobi symbol is defined as

$$\epsilon_n = \begin{cases} 1, & n = 0 \\ 2, & n \neq 0 \end{cases} \tag{39}$$

Eq. (38) was taken from [64] and is a well-known solution of a wave scattering in an infinite domain. In domain-type methods, the infinite domain is truncated by a fictitious surface (cylinder of radius R_e), where Absorbing Boundary Condition is prescribed, and therefore the resulting solution contains an additional boundary truncation

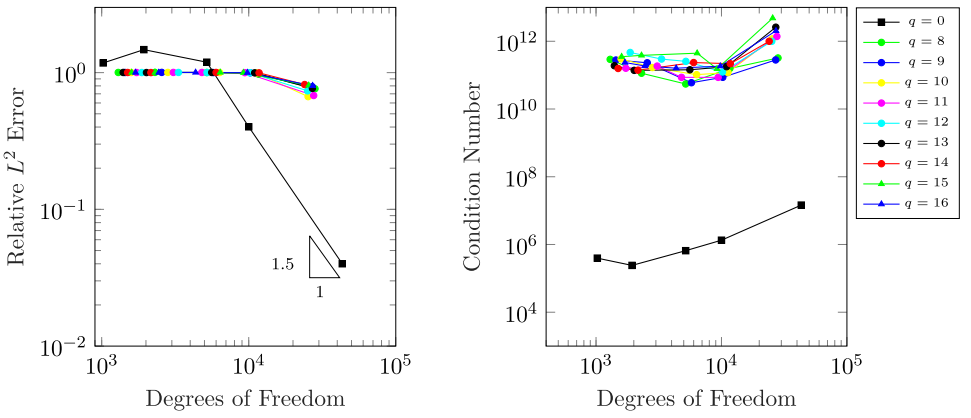

(a) Relative L^2 error. (b) Condition number.

Fig. 40. Spinning wave example: Relative L^2 error norm and condition number study for $p = 3$, $k = 40$ and $m = 42$, varying number of GHP-enrichment functions.

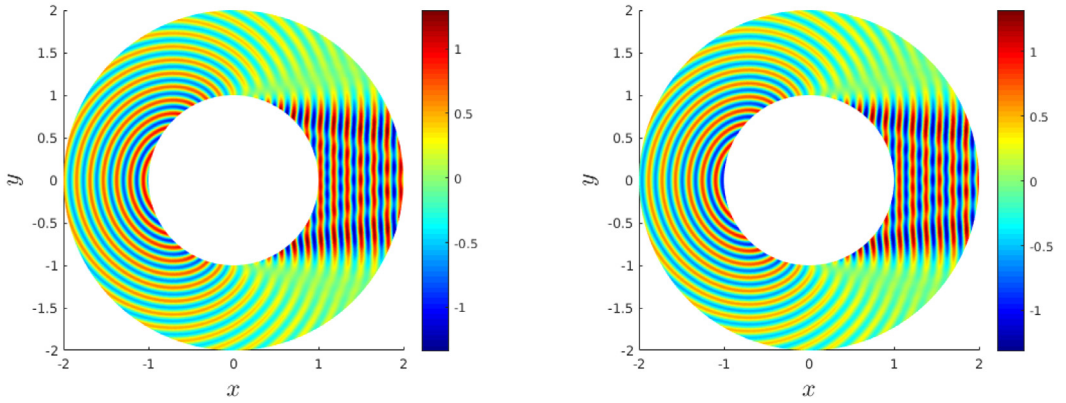

(a) Real part. (b) Imaginary part.

Fig. 41. Analytical solution of wave scattered by a cylinder problem with $k = 40$.

error. Since the focus of this paper is on enrichment and not the ABC error, we consider the following Boundary Value Problem:

Find u such that

$$\Delta u + k^2 u = 0, \qquad \text{in } \Omega \tag{40}$$

$$\frac{\partial u}{\partial n} = f_1, \qquad \text{on } \Gamma_1 \tag{41}$$

$$\frac{\partial u}{\partial n} - \mathrm{i}ku = f_2, \qquad \text{on } \Gamma_2 \tag{42}$$

where functions f_1 and f_2 are derived from a series (Eq. (38)) with 80 terms. The domain Ω and its NURBS parameterization are shown in Fig. 35. In such formulation, both the series truncation and the boundary truncation errors are excluded, and the numerical solution u^h of Problem (40)–(42) converges to its analytical solution. The real and the imaginary parts of the analytical solution for $k = 40$ are shown in Fig. 41.

Figs. 42(a) and 42(b) show the convergent study in terms of relative L^2 error norm vs the DOF, using $p = 3$, $k = 40$ and q from 8 to 16. It can be seen that the PW-enriched IGA-C performs significantly better than the

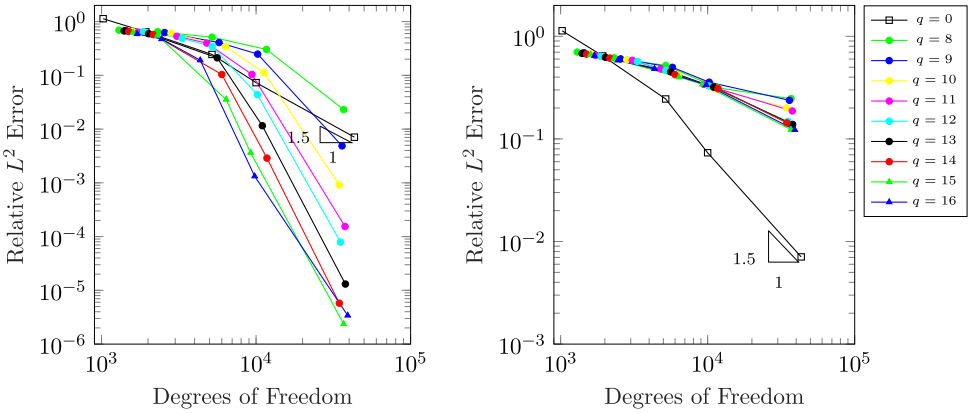

(a) PW-enrichment (b) GHP-enrichment

Fig. 42. Wave scattered by a cylinder: Comparison between the PW- and GHP-enrichment, $p = 3$, $k = 40$.

GHP-enriched IGA-C, bringing up to four order of magnitude improvement in the error on fine meshes, while GHP-enrichment shows worse error than non-enriched IGA-C for all mesh sizes and values of q.

5.5. Star geometry

As a final example, we studied the numerical results for the Helmholtz equation on a star-shaped geometry with a prescribed analytical solution. A five-patch mesh is employed for this example, using the same patch coupling method explained in Section 4.4. The control points and knot vector of each patch are given in Table A.4 from [47].

The following boundary value problem is considered

Find u such that

$$\Delta u + k^2 u = 0, \qquad \text{in } \Omega \tag{43}$$

$$\frac{\partial u}{\partial n} = f_1, \qquad \text{on } \Gamma_N \tag{44}$$

$$\frac{\partial u}{\partial n} - \mathrm{i}ku = f_2, \qquad \text{on } \Gamma_R \tag{45}$$

Like in [77], the prescribed analytical solution is given by:

$$u^{\text{exact}}(\mathbf{x}) = H_0^{(1)}(kr_1(\mathbf{x})) + H_0^{(1)}(kr_2(\mathbf{x})), \tag{46}$$

where $r_1 = |\mathbf{x} - \mathbf{x}_1|$ and $r_2 = |\mathbf{x} - \mathbf{x}_2|$, with $\mathbf{x}_1$ and $\mathbf{x}_2$ inside the interior of the star. In this paper, we used $\mathbf{x}_1 = (0, 1/2)$ and $\mathbf{x}_2 = (0, -1/2)$. Functions f_1 and f_2 are calculated from the analytical solution. The real and the imaginary parts of the analytical solution for $k = 20$ are shown in Fig. 43.

Fig. 44 shows the convergence study in terms of the DOF for both the L^2 error norm and the condition number, using $p = 3$ and q from 8 to 16. In all the simulations, plane-wave enrichment is employed.

In Fig. 45 the same study is repeated with the GHP-enrichment. Both types of enrichment bring significant improvement in the error compared to the non-enriched IGA-C. Interestingly, the condition number in the PW-enriched IGA-C is smaller than in the non-enriched case, while GHP-enrichment leads to much worse conditioning of the system matrix. Large condition number in the GHP-enriched IGA-C case seems to affect the error curves in Fig. 44(a), where the error does not decrease below the order of 10^{-3}. Additionally, error curves for $q \geq 8$ in Fig. 44(a) are close to each other, indicating that adding more GHP-functions in the enriched basis does not bring any improvement, while dependence of the PW-enriched IGA-C error on the number of PW-functions is more pronounced in Fig. 44(a).

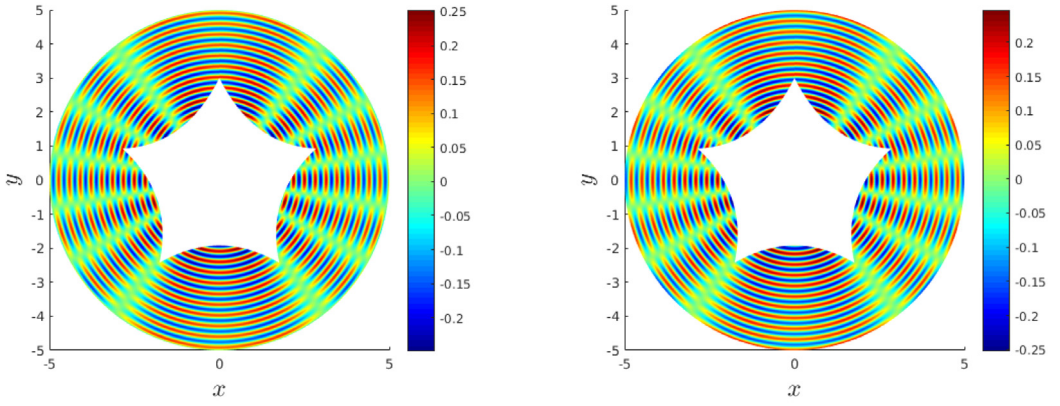

(a) Real part. (b) Imaginary part.

Fig. 43. Analytical solution of sound hard star problem with $k = 20$.

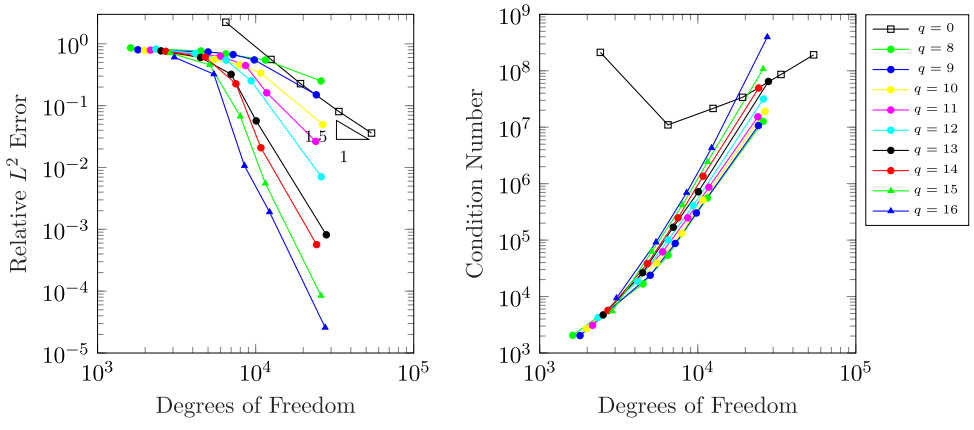

(a) Relative L^2 error. (b) Condition number.

Fig. 44. Star shape example, PW-enrichment: Relative L^2 error norm and condition number study for $p = 3$, $k = 20$, varying number of enrichment functions.

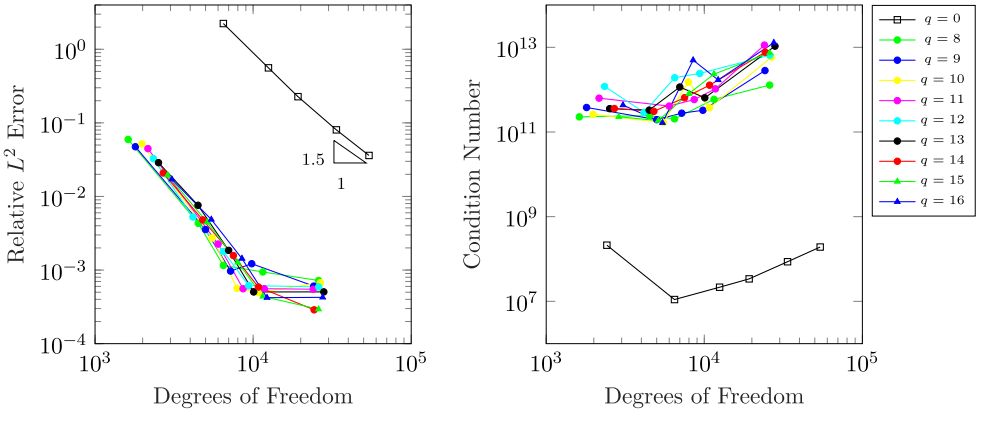

(a) Relative L^2 error. (b) Condition number.

Fig. 45. Star shape example, GHP-enrichment: Relative L^2 error norm and condition number study for $p = 3$, $k = 20$, varying number of enrichment functions.

6. Conclusions

In this work, we showed the application of the Isogeometric Collocation (IGA-C), and Enriched Isogeometric Collocation method to 2D problems for the Helmholtz equation.

First, different collocation schemes were tested for the non-enriched IGA-C, namely, Greville abscissae (GA), Approximated Cauchy-Galerkin (ACG) and Superconvergent points (SC), showing that ACG collocations points are the best choice in terms of the error norm, convergence rate and ease of solving the resulting linear system. Still, in terms of the error per DOF, Galerkin IGA outperforms all of the collocation methods that were tested.

Two types of enrichment, namely Plane Wave (PW-) enrichment and Generalized Harmonic Polynomial (GHP-) enrichment, derived from the general form of the solution of the Helmholtz equation, were tested. In both cases, it was found that in order to achieve maximum efficiency of the method, the number of collocation points needs to be increased beyond the number of unknown degrees of freedom. The most efficient collocation strategy is to add $q+1$ points for PW-enrichment and q for GHP-enrichment, equidistantly between the Approximated Cauchy-Galerkin points (where q is the number of enrichment functions). The resulting non-square matrix must be solved in a least-square sense. In some cases, both types of enrichment improve the overall error by a few orders of magnitude.

The approximation with PW-enrichment is in general superior to that of GHP-enrichment, and the condition number is also smaller, particularly when a large number of enrichments are used. However, for moderately small wave numbers, increasing the number of enrichments does not improve the approximation significantly. On the other hand, if the mesh (i.e. the number of NURBS in the basis before enrichment) is fixed, then the efficiency of enrichment deteriorates if the wave number k is increased. This result means that for larger values of k, more enrichment functions are needed to achieve the same accuracy.

Several multi-patch examples were solved successfully, for both, the standard IGA-C and enriched IGA-C. A simple and effective penalty factor technique was employed on the linear equation system, in order to solve in a least-square sense. However, finding precisely the optimal location of the collocation points for a given number and type of enrichment remains an open problem that can be addressed in a future work.

Acknowledgments

C.A. acknowledges the support of the German Research Foundation (DFG project number 392023639).

References

[1] M. Fink, G. Montaldo, M. Tanter, Time-reversal acoustics in biomedical engineering, Annu. Rev. Biomed. Eng. 5 (1) (2003) 465–497.
[2] P.R. Andersen, V.C. Henríquez, N. Aage, Shape optimization of micro-acoustic devices including viscous and thermal losses, J. Sound Vib. 447 (2019) 120–136.
[3] G. Bao, J. Lai, Radar cross section reduction of a cavity in the ground plane: TE polarization, Discrete Contin. Dyn. Syst. S 8 (3) (2014) 419.
[4] I. Babuška, S. Sauter, Is the pollution effect of the FEM avoidable for the Helmholtz equation considering high wave numbers? SIAM J. Numer. Anal. 34 (6) (1997) 2392–2423.
[5] F. Ihlenburg, I. Babuška, Finite element solution of the Helmholtz equation with high wave number part I: the h-Version of the FEM, Comput. Math. Appl. 30 (9) (1995) 9–37.
[6] F. Ihlenburg, I. Babuška, Finite element solution of the Helmholtz equation with high wave number part II: the h-p version of the FEM, SIAM J. Numer. Anal. 34 (1) (1997) 315–358.
[7] A. Bayliss, M. Gunzburger, E. Turkel, Boundary conditions for the numerical solution of elliptic equations in exterior regions, SIAM J. Appl. Math. 42 (2) (1982) 430–451.
[8] T.J. Hughes, J.A. Cottrell, Y. Bazilevs, Isogeometric analysis: CAD, finite elements, NURBS, exact geometry and mesh refinement, Comput. Methods Appl. Mech. Engrg. 194 (39) (2005) 4135–4195.
[9] J. Cottrell, T.J. Hughes, Y. Bazilevs, Isogeometric Analysis: Toward Integration of CAD and FEA, John Wiley & Sons, 2009.
[10] X. Zhang, C. Jin, P. Hu, X. Zhu, W. Hou, J. Xu, C. Wang, Y. Zhang, Z.-D. Ma, H. Smith, NURBS Modeling and isogeometric shell analysis for complex tubular engineering structures, Comput. Appl. Math. 36 (4) (2017) 1659–1679.
[11] W.A. Wall, M.A. Frenzel, C. Cyron, Isogeometric structural shape optimization, Comput. Methods Appl. Mech. Engrg. 197 (33–40) (2008) 2976–2988.
[12] Y.-D. Seo, H.-J. Kim, S.-K. Youn, Shape optimization and its extension to topological design based on isogeometric analysis, Int. J. Solids Struct. 47 (11–12) (2010) 1618–1640.
[13] B. Hassani, S. Tavakkoli, N. Moghadam, Application of isogeometric analysis in structural shape optimization, Sci. Iran. 18 (4) (2011) 846–852.
[14] Y. Bazilevs, V. Calo, T. Hughes, Y. Zhang, Isogeometric fluid-structure interaction: theory, algorithms, and computations, Comput. Mech. 43 (1) (2008) 3–37.

[15] Y. Bazilevs, M.-C. Hsu, M. Scott, Isogeometric fluid–structure interaction analysis with emphasis on non-matching discretizations, and with application to wind turbines, Comput. Methods Appl. Mech. Engrg. 249 (2012) 28–41.
[16] J. Kiendl, K.-U. Bletzinger, J. Linhard, R. Wüchner, Isogeometric shell analysis with Kirchhoff–Love elements, Comput. Methods Appl. Mech. Engrg. 198 (49–52) (2009) 3902–3914.
[17] D. Benson, Y. Bazilevs, M.-C. Hsu, T. Hughes, Isogeometric shell analysis: the Reissner–Mindlin shell, Comput. Methods Appl. Mech. Engrg. 199 (5–8) (2010) 276–289.
[18] A.J. Herrema, J. Kiendl, M.-C. Hsu, A framework for isogeometric-analysis-based optimization of wind turbine blade structures, Wind Energy 22 (2) (2019) 153–170.
[19] J. Cottrell, A. Reali, Y. Bazilevs, T. Hughes, Isogeometric analysis of structural vibrations, Comput. Methods Appl. Mech. Engrg. 195 (41–43) (2006) 5257–5296.
[20] A. Reali, An isogeometric analysis approach for the study of structural vibrations, J. Earthq. Eng. 10 (2006) 1–30.
[21] S. Shojaee, E. Izadpanah, N. Valizadeh, J. Kiendl, Free vibration analysis of thin plates by using a NURBS-based isogeometric approach, Finite Elem. Anal. Des. 61 (2012) 23–34.
[22] E. De Luycker, D. Benson, T. Belytschko, Y. Bazilevs, M. Hsu, X-FEM In isogeometric analysis for linear fracture mechanics, Internat. J. Numer. Methods Engrg. 87 (6) (2011) 541–565.
[23] S. Ghorashi, N. Valizadeh, S. Mohammadi, Extended isogeometric analysis for simulation of stationary and propagating cracks, Internat. J. Numer. Methods Engrg. 89 (9) (2012) 1069–1101.
[24] S. Ghorashi, N. Valizadeh, S. Mohammadi, T. Rabczuk, Extended isogeometric analysis of plates with curved cracks, in: Civil-Comp Proceedings, vol. 100, 2012.
[25] A. Buffa, G. Sangalli, R. Vázquez, Isogeometric analysis in electromagnetics: B-splines approximation, Comput. Methods Appl. Mech. Engrg. 199 (17) (2010) 1143–1152.
[26] A. Buffa, R. Vázquez, Isogeometric analysis for electromagnetic scattering problems, in: 2014 International Conference on Numerical Electromagnetic Modeling and Optimization for RF, Microwave, and Terahertz Applications (NEMO), IEEE, 2014, pp. 1–3.
[27] L. Coox, E. Deckers, D. Vandepitte, W. Desmet, A performance study of NURBS-based isogeometric analysis for interior two-dimensional time-harmonic acoustics, Comput. Methods Appl. Mech. Engrg. 305 (2016) 441–467.
[28] H. Wu, W. Ye, W. Jiang, Isogeometric finite element analysis of interior acoustic problems, Appl. Acoust. 100 (2015) 63–73.
[29] T. Khajah, X. Antoine, S.P. Bordas, B-spline FEM for time-harmonic acoustic scattering and propagation, J. Theoret. Comput. Acoust. (2019) 1850059.
[30] V.P. Nguyen, C. Anitescu, S.P. Bordas, T. Rabczuk, Isogeometric analysis: an overview and computer implementation aspects, Math. Comput. Simulation 117 (2015) 89–116.
[31] G. Beer, S. Bordas, et al., Isogeometric Methods for Numerical Simulation, vol. 240, Springer, 2015.
[32] R. Simpson, M. Scott, M. Taus, D. Thomas, H. Lian, Acoustic isogeometric boundary element analysis, Comput. Methods Appl. Mech. Engrg. 269 (2014) 265–290.
[33] L. Chen, H. Lian, Z. Liu, H. Chen, E. Atroshchenko, S. Bordas, Structural shape optimization of three dimensional acoustic problems with isogeometric boundary element methods, Comput. Methods Appl. Mech. Engrg. 355 (2019) 926–951.
[34] F. Auricchio, L.B. Da Veiga, T. Hughes, A. Reali, G. Sangalli, Isogeometric collocation methods, Math. Models Methods Appl. Sci. 20 (11) (2010) 2075–2107.
[35] F. Auricchio, L.B. Da Veiga, T.J. Hughes, A. Reali, G. Sangalli, Isogeometric collocation for elastostatics and explicit dynamics, Comput. Methods Appl. Mech. Engrg. 249 (2012) 2–14.
[36] H. Lin, Q. Hu, Y. Xiong, Consistency and convergence properties of the isogeometric collocation method, Comput. Methods Appl. Mech. Engrg. 267 (2013) 471–486.
[37] D. Schillinger, J.A. Evans, A. Reali, M.A. Scott, T.J. Hughes, Isogeometric collocation: cost comparison with Galerkin methods and extension to adaptive hierarchical NURBS discretizations, Comput. Methods Appl. Mech. Engrg. 267 (2013) 170–232.
[38] L. da Veiga, C. Lovadina, A. Reali, Avoiding shear locking for the Timoshenko beam problem via isogeometric collocation methods, Comput. Methods Appl. Mech. Engrg. 241 (2012) 38–51.
[39] F. Auricchio, L.B. da Veiga, J. Kiendl, C. Lovadina, A. Reali, Locking-free isogeometric collocation methods for spatial Timoshenko rods, Comput. Methods Appl. Mech. Engrg. 263 (2013) 113–126.
[40] A. Reali, H. Gomez, An isogeometric collocation approach for Bernoulli–Euler beams and Kirchhoff plates, Comput. Methods Appl. Mech. Engrg. 284 (2015) 623–636.
[41] J. Kiendl, F. Auricchio, L.B. da Veiga, C. Lovadina, A. Reali, Isogeometric collocation methods for the Reissner–Mindlin plate problem, Comput. Methods Appl. Mech. Engrg. 284 (2015) 489–507.
[42] L.D. Lorenzis, J. Evans, T. Hughes, A. Reali, Isogeometric collocation: Neumann boundary conditions and contact, in: Isogeometric Analysis Special Issue, Comput. Methods Appl. Mech. Engrg. 284 (2015) 21–54.
[43] R.W. Johnson, Higher order B-spline collocation at the Greville abscissae, Appl. Numer. Math. 52 (1) (2005) 63–75.
[44] C. Anitescu, Y. Jia, Y.J. Zhang, T. Rabczuk, An isogeometric collocation method using superconvergent points, Comput. Methods Appl. Mech. Engrg. 284 (2015) 1073–1097.
[45] H. Gomez, L. De Lorenzis, The variational collocation method, Comput. Methods Appl. Mech. Engrg. 309 (2016) 152–181.
[46] M. Montardini, G. Sangalli, L. Tamellini, Optimal-order isogeometric collocation at Galerkin superconvergent points, Comput. Methods Appl. Mech. Engrg. 316 (2017) 741–757.
[47] J. Videla, C. Anitescu, T. Khajah, S.P. Bordas, E. Atroshchenko, H- and p-adaptivity driven by recovery and residual-based error estimators for PHT-splines applied to time-harmonic acoustics, Comput. Math. Appl. 77 (9) (2019) 2369–2395.
[48] A. Lieu, G. Gabard, H. Bériot, A comparison of high-order polynomial and wave-based methods for Helmholtz problems, J. Comput. Phys. 321 (2016) 105–125, http://dx.doi.org/10.1016/j.jcp.2016.05.045.

[49] H. Bériot, A. Prinn, G. Gabard, Efficient implementation of high-order finite elements for Helmholtz problems, Internat. J. Numer. Methods Engrg. 106 (3) (2016) 213–240.
[50] K. Christodoulou, O. Laghrouche, M. Mohamed, J. Trevelyan, High-order finite elements for the solution of Helmholtz problems, Comput. Struct. 191 (2017) 129–139.
[51] A.E. Kacimi, O. Laghrouche, M. Mohamed, J. Trevelyan, Bernstein–Bézier based finite elements for efficient solution of short wave problems, Comput. Methods Appl. Mech. Engrg. 343 (2019) 166–185.
[52] J. Melenk, I. Babuška, The partition of unity finite element method: basic theory and applications, Comput. Methods Appl. Mech. Engrg. 139 (1–4) (1996) 289–314.
[53] I. Babuška, J.M. Melenk, The partition of unity method, Internat. J. Numer. Methods Engrg. 40 (4) (1997) 727–758.
[54] M. Mohamed, O. Laghrouche, A. El-Kacimi, Some numerical aspects of the PUFEM for efficient solution of 2D Helmholtz problems, Comput. Struct. 88 (23–24) (2010) 1484–1491.
[55] T. Strouboulis, I. Babuška, R. Hidajat, The generalized finite element method for Helmholtz equation: theory, computation, and open problems, Comput. Methods Appl. Mech. Engrg. 195 (37–40) (2006) 4711–4731.
[56] T. Strouboulis, R. Hidajat, I. Babuška, The generalized finite element method for Helmholtz equation. Part II: Effect of choice of handbook functions, error due to absorbing boundary conditions and its assessment, Comput. Methods Appl. Mech. Engrg. 197 (5) (2008) 364–380.
[57] R. Hiptmair, A. Moiola, I. Perugia, A survey of Trefftz methods for the Helmholtz equation, in: G.R. Barrenechea, F. Brezzi, A. Cangiani, E.H. Georgoulis (Eds.), Building Bridges: Connections and Challenges in Modern Approaches To Numerical Partial Differential Equations, Springer International Publishing, Cham, 2016, pp. 237–279.
[58] P. Bettess, O. Laghrouche, E. Perrey-Debain, E. Perrey-Debain, O. Laghrouche, P. Bettess, J. Trevelyan, Plane-wave basis finite elements and boundary elements for three-dimensional wave scattering, Phil. Trans. R. Soc. A 362 (1816) (2004) 561–577.
[59] M.J. Peake, J. Trevelyan, G. Coates, Extended isogeometric boundary element method (XIBEM) for two-dimensional Helmholtz problems, Comput. Methods Appl. Mech. Engrg. 259 (2013) 93–102.
[60] M. Peake, J. Trevelyan, G. Coates, Extended isogeometric boundary element method (XIBEM) for three-dimensional medium-wave acoustic scattering problems, Comput. Methods Appl. Mech. Engrg. 284 (2015) 762–780.
[61] M. Dinachandra, S. Raju, Plane wave enriched partition of unity isogeometric analysis (PUIGA) for 2D-Helmholtz problems, Comput. Methods Appl. Mech. Engrg. 335 (2018) 380–402.
[62] G.C. Diwan, M.S. Mohamed, Pollution studies for high order isogeometric analysis and finite element for acoustic problems, Comput. Methods Appl. Mech. Engrg. 350 (2019) 701–718.
[63] A. El Kacimi, O. Laghrouche, Improvement of PUFEM for the numerical solution of high-frequency elastic wave scattering on unstructured triangular mesh grids, Internat. J. Numer. Methods Engrg. 84 (3) (2010) 330–350.
[64] S. Banerjee, N. Sukumar, Exact integration scheme for planewave-enriched partition of unity finite element method to solve the Helmholtz problem, Comput. Methods Appl. Mech. Engrg. 317 (2017) 619–648.
[65] N. Moës, J. Dolbow, T. Belytschko, A finite element method for crack growth without remeshing, Internat. J. Numer. Methods Engrg. 46 (1) (1999) 131–150.
[66] D.J. Benson, Y. Bazilevs, E. De Luycker, M.-C. Hsu, M. Scott, T. Hughes, T. Belytschko, A generalized finite element formulation for arbitrary basis functions: from isogeometric analysis to XFEM, Internat. J. Numer. Methods Engrg. 83 (6) (2010) 765–785.
[67] X. Peng, E. Atroshchenko, P. Kerfriden, S. Bordas, Isogeometric boundary element methods for three dimensional static fracture and fatigue crack growth, Comput. Methods Appl. Mech. Engrg. 316 (2017) 151–185.
[68] M. Drolia, M. Mohamed, O. Laghrouche, M. Seaid, J. Trevelyan, Enriched finite elements for initial-value problem of transverse electromagnetic waves in time domain, Comput. Struct. 182 (2017) 354–367.
[69] M. Mahmood, O. Laghrouche, J. Trevelyan, A.E. Kacimi, Implementation and computational aspects of a 3D elastic wave modelling by PUFEM, Appl. Math. Model. 49 (2017) 568–586.
[70] E. Atroshchenko, S. Tomar, G. Xu, S.P. Bordas, Weakening the tight coupling between geometry and simulation in isogeometric analysis: from sub- and super-geometric analysis to geometry-independent field approximation (GIFT), Internat. J. Numer. Methods Engrg. 114 (10) (2018) 1131–1159.
[71] L. Piegl, W. Tiller, The NURBS Book, Springer Science & Business Media, 2012.
[72] O. Zienkiewicz, J. Zhu, The superconvergent patch recovery and a posteriori error estimates. Part 1: the recovery technique, Internat. J. Numer. Methods Engrg. 33 (7) (1992) 1331–1364.
[73] O. Zienkiewicz, J. Zhu, The superconvergent patch recovery and *a posteriori* error estimates. Part 2: error estimates and adaptivity, Internat. J. Numer. Methods Engrg. 33 (7) (1992) 1365–1382.
[74] T. Huttunen, P. Gamallo, R. Astley, Comparison of two wave element methods for the Helmholtz problem, Commun. Numer. Methods. Eng. 25 (1) (2009) 35–52.
[75] J. Videla, F. Contreras, H.X. Nguyen, E. Atroshchenko, Application of PHT-splines in bending and vibration analysis of cracked Kirchhoff-Love Plates, Comput. Methods Appl. Mech. Engrg. 361 (2020) 112754.
[76] C. Farhat, I. Harari, L.P. Franca, The discontinuous enrichment method, Comput. Methods Appl. Mech. Engrg. 190 (48) (2001) 6455–6479.
[77] V. Villamizar, S. Acosta, B. Dastrup, High order local absorbing boundary conditions for acoustic waves in terms of farfield expansions, J. Comput. Phys. 333 (2017) 331–351.